



LUND UNIVERSITY

---

# Simulation of Majorana Bound States in Multi-Band Josephson Junction Nanowires

---

*Author:*

Georg Wolgast

*Supervisor:*

Martin Leijnse

*Co-supervisor:*

Michael Hell

## Abstract

Majorana bound states can be created at the ends of semiconducting nanowires using a combination of proximity-induced superconductivity, spin-orbit coupling and a magnetic field. By adding a Josephson junction to this nanowire, four Majorana bound states can exist at the same time in the system. In this thesis I aim to examine the impact that the barrier in Josephson junctions has on the energy states in multi-band nanowires. This is done through simulations using a tight-binding model. The thesis will focus on how Majorana bound states in the system will be influenced by different widths and heights of the Josephson junction barrier through calculations of the Majorana coupling energy and the energy gap to the nearest excited state. By choosing a larger barrier width the system will require a smaller voltage to achieve four Majorana bound states, but be more susceptible to changes in the excited states. This result will only appear in multi-band models. The study indicates that Majorana bound states will behave differently in different energy bands and that the choice of barrier width is non-trivial in order to avoid influences from excited states.

April 11, 2017

## CONTENTS

I. Introduction	1
A. Majorana Theory	1
B. Quantum Computing	2
C. Purpose of Thesis	2
II. Theory	2
A. Superconductivity	2
B. Spin-Orbit Coupling	3
C. Practical Implementation	3
D. Finite Wire	5
III. Tight-Binding model	6
A. Simple Nanowire	6
B. Nanowire With Josephson Junction	8
IV. Multi-Band model	11
A. Two-Band Model	11
B. Three-Band Model	16
V. Multi-Band Josephson Junction	22
A. Barrier Data	22
B. Discussion	24
VI. Outlook and Conclusions	25
Acknowledgements	25
References	26
A. Barrier Shapes	27
1. Trapezoidal Barrier	27
2. Triangular Barrier	29

## I. INTRODUCTION

## A. Majorana Theory

Majorana bound states in topological superconductors are a rapidly growing research field with possible uses in the field of quantum computing [1]. In particle physics, a Majorana fermion is defined as a fermionic particle that is its own anti-particle [2].

Majorana fermions are neutral half-integer-spin particles with only real components to their wavefunctions. This is what defines it as its own anti-particle, as an anti-particle's wavefunction is the complex conjugate of the particle's [3]. It is in contrast to Dirac fermions, such as electrons or protons, that have both a real and an imaginary part to their wavefunctions.

It is unclear if there exist any elementary particles that are Majorana fermions, however in condensed matter physics they can exist as quasiparticle excitations in superconductors and form Majorana bound states at the middle of the superconducting gap at zero energy [2]. Majorana bound states will form at the ends of nanowires, see Fig. 1.



FIG. 1: A schematic sketch of the Majorana bound states in a nanowire. The X's are Majorana bound states at the ends of the wire.

In condensed matter physics, Majorana bound states are an interesting field of research because of their exotic exchange statistics. They are non-Abelian anyons [4], meaning that multiple exchanges of different Majorana bound states will change the state of the total system in a way that depends on the order that the exchanges were done in. In other words, exchanges of particles will lead to a linear, non-commuting transformation of the system. This means that in a degenerate state, exchanges can transform the system from one state into another one [5].

Majorana operators (here written as  $\gamma$ ) are Hermitian  $\gamma^\dagger = \gamma$ , meaning that a Majorana bound state is equal to its own hole. This also means that Majorana operators are both creation and annihilation operators at the same time, another quality unique to Majoranas. The anti-commutation relations of Majorana operators are given by [2]

$$\{\gamma_i, \gamma_j\} = 2\delta_{ij}, \quad (1)$$

where  $\delta_{ij}$  is a Krönicker-delta. From (1), we see that  $\gamma_i^2 = 1$ , which does not follow the Pauli principle for Dirac fermions. In fact there is no Pauli principle for Majoranas, because a Majorana mode cannot be occupied in a traditional way. Because Majorana creation operators are also annihilation operators, Majorana modes are always filled and always empty at the same time [2].

A fermionic state can be created by a superposition of two Majorana bound states

$$f^\dagger = \frac{\gamma_1 - i\gamma_2}{\sqrt{2}}, \quad (2)$$

where  $f^\dagger$  is a fermionic creation operator and  $\gamma_1$  and  $\gamma_2$  are Majorana field operators. Another reason to investigate Majorana bound states is the nature of this superposition. A property of this superposition is that the Majorana bound states can be spatially separated. This can lead to a quantum state where the Majorana bound states that define the fermionic state are separated enough to be protected from local perturbations. The specific details of this protection will be explained later in Section IID. Perturbations are changes to the system, which can lead to decoherence. Decoherence can be explained as a loss of quantum information to the system's environment, eventually effectively destroying the quantum coherence of the state. This is usually undesirable, especially for quantum computing systems as the purpose of the states in those systems is to store information.

## B. Quantum Computing

Nanowires with Majorana bound states at the ends can be used to create qubits, a key component in quantum computers. A bit is what computers use to store information, it can be either 1 or 0. In ordinary computers, the distinction between a 1 and a 0 is given by voltage, high voltage is a 1, low voltage is a 0. In quantum computers using Majorana bound states, this distinction is instead made by the occupation of different fermionic states. The fermionic state created by the two Majorana bound states at the ends of the wire  $\gamma_1$  and  $\gamma_N$  can either be occupied or not, leading to quantum states defined as  $|0\rangle$  meaning non-occupied and  $|1\rangle$  meaning occupied. The problem with using these definitions to define a qubit is that  $|0\rangle$  corresponds to a system with an even number of fermions and  $|1\rangle$  corresponds to a system with an odd number of fermions. This makes it impossible to change between the different states in a closed system, so a different definition is used.

By adding two more Majorana bound states to the system, another fermionic state can be created and four possible combinations of states can be formed:  $|00\rangle$ ,  $|01\rangle$ ,  $|10\rangle$  and  $|11\rangle$ . By choosing to define a qubit 0 representation as  $|00\rangle$  and a qubit 1 representation as  $|11\rangle$  corresponding to either none or both of the fermionic states being occupied, the fermion number parity of the system is conserved when changing between these states as both will correspond to a system with an even number of fermions [6]. In order to add two more Majorana bound states to the system, a Josephson junction is used.

## C. Purpose of Thesis

In this thesis I will look at models for nanowire Josephson junction systems that are currently being manufactured and simulate them with respect to different parameter choices [7, 8]. I will first use a single-band tight-binding model with a solid piece of superconductor. A Josephson junction will then be introduced in order to investigate how Majorana bound states in these systems can be manipulated by using gate electrodes to control the wavefunction overlap in Josephson junctions. Next, the model will be extended by making a more realistic nanowire with several energy band levels. Both a two- and a three-band model will be simulated. Finally an investigation is done on how the size and shape of the Josephson junction will affect the Majorana bound states' overlap in this extended model.

The Josephson junction system is an interesting experimental set-up for Majorana research and more analysis of different parameters' influence on the Majorana bound states, such as the width of the gap between the superconducting sections as well as the gate voltage, can prove useful for future experiments. In that interest, I have used material parameters for InAs, a material commonly used in research.

## II. THEORY

### A. Superconductivity

In order to create Majorana bound states, a superconductor is required. A superconductor is a material that electrons can move through without resistance. This is because electrons in superconductors are superfluids, meaning that they can flow without energy dissipation. This superfluid is made up of Cooper pairs, two electrons that have an attractive interaction with each other and have therefore paired up. In conventional superconductors, this attractive force is due to electron-phonon interactions. This interaction can be qualitatively illustrated by the following example [9]. As a negatively charged electron moves through a lattice of positively charged ions that comes from the superconducting material, the ions are attracted to the electron and are shifted towards it. This will cause a second electron to be attracted towards this cluster of ions, leading to an effective attraction between the electrons. At a low enough temperature, this attractive force will overcome the repulsive Coulomb interactions between the electrons and they will become paired as Cooper pairs. These pairs will then form a condensate where all pairs have the same phase, creating a superconductor.

This coupling of electrons leads to some important effects, one of them being the superconducting gap. In order to excite a single electron and split a Cooper pair, energy is required to overcome the electrons' attractive force. This leads to an energy gap for single-particle excitation called the superconducting gap. This superconducting gap is an important characteristic of superconductors.

There are different types of superconductors depending on the angular momentum  $l$  of the Cooper pair wavefunction. An s-wave superconductor will have  $l = 0$ , has an isotropic superconducting gap and spin-singlet pairing, which means that Cooper pairs will form with electrons with opposite spin [10]. This is the most common type of superconductor. A p-wave superconductor will have  $l = 1$  and a spin-triplet pairing, meaning that Cooper pairs will form with electrons with same spin [11]. The specific p-wave superconductor that is relevant for Majorana physics is the  $p_x + ip_y$  superconductor which has a superconducting gap given by

$$\Delta \propto (p_x + ip_y), \quad (3)$$

where  $\Delta$  is the superconducting gap, and  $p_x$  and  $p_y$  are the momentum in  $x$ - and  $y$ -direction, respectively [12].

Majorana bound states are by definition spinless [13]. In order to have a spinless superconductor the Cooper pairs must have antisymmetric wavefunctions. This is not possible in an s-wave superconductor, so therefore a p-wave superconductor is required in order to have Majorana bound states. However, p-wave superconductors are very rare, so it would be helpful to in some way make

s-wave superconductors behave like a  $p_x + ip_y$  superconductor. Luckily, this is possible as shown in [14] by using proximity-induced superconductivity from a s-wave superconductor.

Proximity-induced superconductivity can happen when a superconductor (S) comes into electrical contact with a normal material (N). The Cooper pairs in the superconductor will not simply disappear at the S-N interface, but instead leak into the normal material, creating Cooper pairs from N's unpaired electrons. This will make N behave as a superconductor [15, 16].

## B. Spin-Orbit Coupling

Spin-orbit coupling is the interaction of a particle's spin with its orbital environment. In a semiconductor there is inversion asymmetry, which leads to a specific kind of spin-orbit coupling called Rashba spin-orbit coupling. This will lead to a spin-splitting effect, which splits the energy bands with momentum-dependent spin directions [17]. The spin-orbit will enter the Hamiltonian as spin-orbit coupling strength  $\alpha$  given by [18]

$$\alpha = \alpha_R/2a, \quad (4)$$

where  $a$  is the lattice spacing and  $\alpha_R$  is the Rashba coupling which is determined experimentally.  $\alpha_R$  was supposed to be  $\alpha_R = 8 \text{ peV m}$  [19, 20] but due to a coding mistake was instead set to  $\alpha_R = 16 \text{ peV m}$ . This is however still within the experimental range.

## C. Practical Implementation

As mentioned previously, Majorana bound states can be created using proximity-induced superconductivity in semiconductors with spin-orbit coupling [21]. This can be achieved by placing a semiconductor nanowire in close contact with a superconductor. By applying a magnetic field to this structure, Majorana bound states can be found at the ends of the nanowire, see Fig. 1 in Section IA. In order to find Majorana bound states in the system, the chemical potential of the system has to be within a specific energy range. In an experimental set-up, it is therefore necessary to include a gate electrode in order to be able to tune the chemical potential of the system. A sketch of an experimental set-up can be seen in Fig. 2.

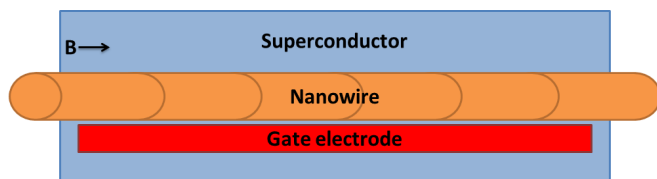


FIG. 2: A top-down view of an experimental set-up.

An intuitive picture of why Majorana bound states are formed at the ends of the wire is given by the Kitaev model [22] which is illustrated in Fig. 3. The nanowire can be modeled as a chain of fermions with fixed spin, each corresponding to two Majorana bound states as in (2), see Fig. 3a. By adding superconducting pairing and the ability for electrons to hop between sites to this nanowire, as well as having specific parameter choices, these fermions will instead be formed by combining one Majorana bound state from each original fermion, see Fig. 3b for an illustration and [22] for a full explanation. This will leave a Majorana bound state at each end unpaired, thereby creating Majorana bound states that will be separated by the length of the nanowire.

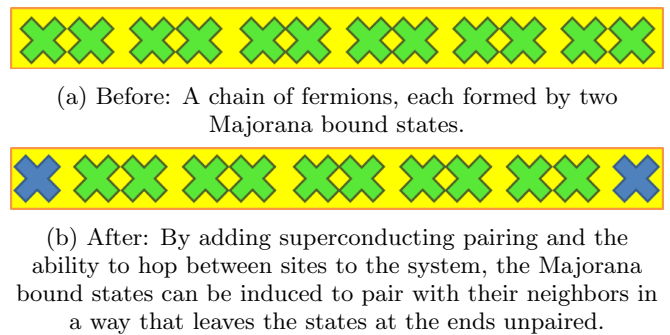


FIG. 3: A schematic of the Kitaev model. The green X's are paired Majorana bound states that together create a fermion.

In order to achieve Majorana bound states, a magnetic field and spin-orbit coupling is required. In order to illustrate the impact that these factors will have on the energy band structure, a model was created for an infinitely long nanowire. This model has taken the Hamiltonian in (15) and made the ansatz that in an infinitely long wire the solution to the Schrödinger equation will be given by a plane wave

$$\psi = e^{-ikx}, \quad (5)$$

where  $k$  is a wave vector. This is equivalent to mathematically performing a Fourier transform of (15). By doing the same matrix transformation as in (18), the following matrix was constructed. More information regarding (15) and how (6) was calculated can be found in Section III A.

$$\begin{bmatrix} -\mu + \frac{\hbar^2 k^2}{2m^*} & h_x + i\alpha_R k & \Delta & 0 \\ h_x - i\alpha_R k & -\mu + \frac{\hbar^2 k^2}{2m^*} & 0 & \Delta \\ \Delta & 0 & \mu - \frac{\hbar^2 k^2}{2m^*} & h_x + i\alpha_R k \\ 0 & \Delta & h_x - i\alpha_R k & \mu - \frac{\hbar^2 k^2}{2m^*} \end{bmatrix} \quad (6)$$

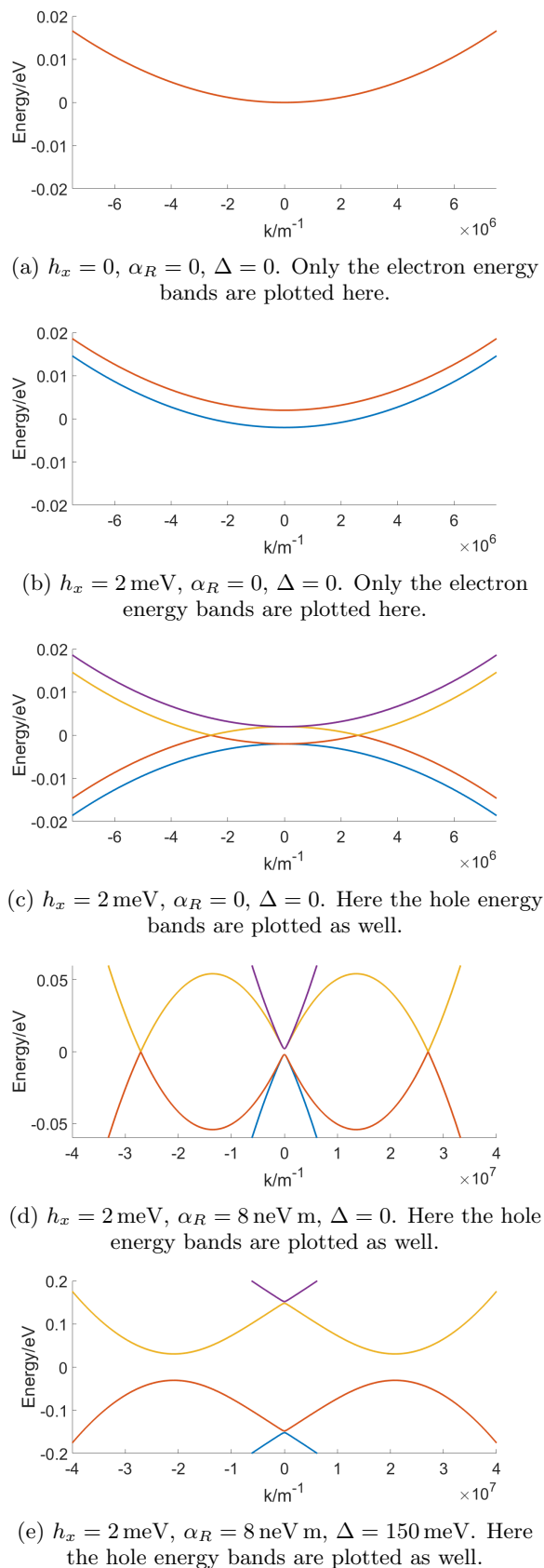


FIG. 4: Energy bands depending on different parameters. These plots have been calculated by diagonalizing (6) with  $\mu = 0$  and  $m^* = 0.023 m_e$ .

Starting from a quasi free-electron model, the dispersion relation is given by

$$H = \frac{\hbar^2 k^2}{2m^*}, \quad (7)$$

where  $\hbar$  is Planck's reduced constant and  $m^*$  is the effective electron mass. This relation is what gives the parabola in Fig. 4a. Majorana bound states cannot exist in a spin-degenerate energy band because then two Majorana bound states can form in each degenerate state and then combine to form a fermion according to (2). Therefore the energy bands will need to separate using a magnetic field to introduce Zeeman splitting. The Zeeman energy gap seen at  $k = 0$  is given by

$$h_x = g\mu_B B/2, \quad (8)$$

where  $h_x$  is the Zeeman energy gap,  $g$  is the Landé g-factor,  $\mu_B$  is the Bohr magneton and  $B$  is the applied magnetic field strength. The energy bands with and without Zeeman splitting can be seen in Fig. 4a and Fig. 4b. This generates a non-spin-degenerate energy band. In order to see the other effects, the hole energy bands are included in Fig. 4c. Adding in the spin-orbit term and looking at the hole bands as well as the electron bands, a Zeeman energy gap will still appear at  $k = 0$ , see Fig. 4d.

As s-wave superconductivity is added to this system Cooper pairs will form within the same energy band. These Cooper pairs will need to pair electrons with different spins, however these will not be available without spin-orbit coupling. Adding both spin-orbit coupling and superconductivity allows for each state in the energy band to be a superposition of different spins, thereby allowing Cooper pairs to be formed from electrons with different spin in the same non-spin-degenerate energy band. This is how an effective p-wave superconductor can be created with proximity-induced s-wave superconductivity. The superconductivity will lead to a two new energy gaps in the system at  $k = \pm 2 \cdot 10^7 \text{ m}^{-1}$ , see Fig. 4e [23]. These energy gaps are called the topological energy gap. As the magnetic field is increased, the gap at  $k = \pm 2 \cdot 10^7 \text{ m}^{-1}$  will close and a topological phase transition will happen at

$$h_x = \sqrt{\Delta^2 + \mu^2}, \quad (9)$$

where  $\Delta$  is the induced superconducting gap and  $\mu$  is the chemical potential [2].

By creating this energy band structure Cooper pairs of same spin electrons will form, the same kind found in p-wave superconductors. This allows Majorana bound states to be able to exist in the system, as long as only one of the Zeeman split energy subbands are occupied. As soon as the chemical potential allows for electrons in the second split energy subband spin-degeneracy will be introduced to the system, thereby breaking the Majorana bound states.

### D. Finite Wire

If the wire has finite length, the Majorana bound states at the ends of the wire will have weak interaction proportional to  $w$  given by [22, 24]

$$w \propto e^{-L/l_0} \cos k_F L, \quad (10)$$

where  $w$  is the cost in energy to occupy the resulting fermionic state that the interacting Majorana bound states will create,  $L$  is the length of the wire,  $l_0$  is the length scale over which the Majorana bound state's wavefunction decays and  $k_F$  is an effective Fermi wave vector.  $w$  can be minimized by making the wire as long as possible, however as this term will oscillate as a function of  $k_F(h_x, \mu)$ , there is a way to make this term zero. The magnetic field in the system will influence  $k_F$ , causing interference which at certain values of  $h_x$  will lead to zero overlap.

A Hamiltonian for these edge Majorana bound states is given by [25, 26]

$$H = E_0 \sigma_z, \quad (11)$$

where  $E_0$  is an energy proportional to  $w$  and therefore also proportional to the overlap of the edge states ( $\gamma_1$  and  $\gamma_N$ ) and  $\sigma_z$  is a Pauli matrix. The basis for the Pauli matrix are the states  $|00\rangle$  and  $|11\rangle$  mentioned in Section IB.

Changes in the environment, for example fluctuations in  $\mu$  or the magnetic field, will cause the system to evolve differently in time depending on  $E_0$ . This means that a measurement of the state can give different results depending on the time of the measurements. If  $E_0$  fluctuates, this will mean that the system will evolve in an unpredictable way and it will lose coherence as it evolves in time. For example, if one prepares a system in the state  $|00\rangle + |11\rangle$  and let it evolve in time with a fluctuating  $E_0$ , the phase between  $|00\rangle$  and  $|11\rangle$  is no longer well defined and it becomes impossible to say what state the system was in originally. However, if  $E_0 = 0$  this means that a measurement will always yield the same result, thereby creating a system that is protected from decoherence [27]. As  $E_0$  is proportional to the overlap of the Majorana bound states, this means that it is very important to keep the overlap as low as possible when trying to store quantum information. Zero overlap is not possible in a finite system according to (10) except for certain values of  $h_x$ . This means that it is hard to maintain  $E_0 = 0$  as a small change to the system will cause  $E_0$  to be finite again.

Since each nanowire in the above example can host two Majorana bound states, a qubit that needs four Majorana bound states can be constructed using two nanowires. However in order for that qubit to be useful for quantum computations, one needs to be able to manipulate the qubit and couple it to other qubits. That means that one needs to combine two nanowires in a way that allows for the different Majorana bound states to interact with

each other. An interaction can for example be to allow for two Majorana bound states' wavefunctions to overlap in a controlled manner, this will change  $E_0$ . This change can be detected and used for a qubit operation.

A practical way to create a system that behaves as two separate nanowires is to split a nanowire into two parts using a Josephson junction. A Josephson junction is defined by two superconductors separated by a thin layer of non-superconducting material. Since the wire that is used is ordinarily a semiconductor and is only superconducting due to proximity-induced effects, one can create a Josephson junction by simply making two ends of the wire superconducting and leaving the middle as a semiconductor, see Fig. 5. This means that a single nanowire is split into two separate parts, each with two Majorana bound states.

Applying a voltage in the middle of the wire effectively creates an energy barrier or energy well. A barrier allows a separation of the two parts of the wire which can be manipulated and the overlap of the Majorana bound state's wavefunction can be controlled. This can be used as a qubit operation, using voltage to control whether the Majorana bound states can interact or not. This is an advantage of using a semiconductor instead of an insulator as a separator in the Josephson junction, as a semiconductor can be more easily manipulated. The Majorana bound states at the edge of the Josephson junction will slightly overlap depending on the shape of the Josephson junction, creating a new Hamiltonian [25, 26]

$$H = E_0 \sigma_z + E_M \sigma_x, \quad (12)$$

where  $\sigma_z$  and  $\sigma_x$  are Pauli matrices like the one in (11).  $E_M$  is the Majorana coupling energy proportional to the overlap between the Majorana bound states closest to the Josephson junction ( $\gamma_{j1}$  and  $\gamma_{j2}$ ). By manipulating the Josephson junction it is possible to adjust  $E_M$ , controlling whether the Majorana bound states can interact or not. Once again if one wishes to avoid loss of information it is important to make this overlap as small as possible in order to minimize  $E_M$  for the non-interacting (off) case.

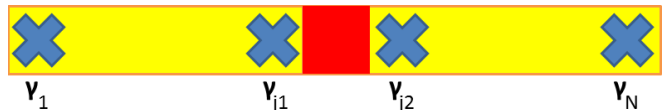


FIG. 5: A schematic of the Majorana bound states when the system has a Josephson junction. The red block in the middle represents the part of the wire that is not superconducting.

This is of course only one way to define a qubit operation on this system. As explained above, allowing the wavefunctions of Majorana bound states to overlap, even in a controlled manner, can cause decoherence. A more robust method is to define a qubit operation as the physical exchange of the two Majorana bound states. Because

of their non-Abelian exchange statistics, this will change the system in a way that can be detected. This is beyond the scope of this thesis, but more details can be found in [26].

### III. TIGHT-BINDING MODEL

In order to study Majorana bound states in a nanowire, a tight-binding model coded in MATLAB was developed. This discretizes the nanowire into finite lattice points and approximates the Hamiltonian as a finite size matrix. The wavefunctions are found by diagonalizing the Hamiltonian matrix and solving the standard eigenvalue problem of

$$H_{ij}\vec{\Psi} = E\vec{\Psi}, \quad (13)$$

where the Hamiltonian matrix  $H_{ij}$  has eigenvectors corresponding to the wavefunctions  $\Psi$  and eigenstates corresponding to the energies  $E$ . A Nambu spinor was chosen to describe the wavefunction in order to include both electrons and holes explicitly. This is a standard spinor for superconducting systems since there is electron-hole symmetry in these systems;

$$\vec{\Psi} = (\Psi_{\uparrow}, \Psi_{\downarrow}, \Psi_{\downarrow}^{\dagger}, -\Psi_{\uparrow}^{\dagger})^T \quad (14)$$

where every  $\Psi$  is a vector with length  $N$ ,  $\uparrow/\downarrow$  denotes different spins and  $\dagger$  denotes hole states.

If the nanowire is discretized into  $N$  lattice points, the wavefunction will be represented by a  $4N$ -dimensional vector where each lattice point has 4 corresponding values of the wavefunction, one for each term in the Nambu spinor inserted sequentially as written in (14). Similarly, the Hamiltonian matrix will be a  $4N \times 4N$  matrix where each lattice point is represented by a  $4 \times 4$  matrix on the diagonal that describes the different electron/hole spins' interaction with each other.

#### A. Simple Nanowire

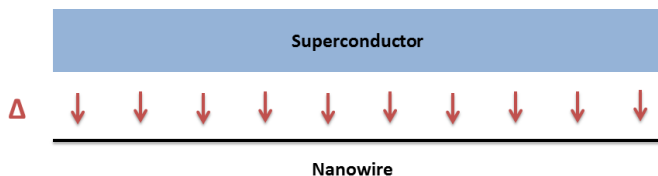


FIG. 6: A schematic of the nanowire system. Note that the superconductor covers the entire wire and induces superconductivity in the whole system.

The first system looked at was a simple one-dimensional spin-orbit coupled nanowire with proximity-induced superconductivity and a magnetic field along the

wire. A schematic of the system can be seen in Fig. 6. The Hamiltonian of the system can be expressed as [28]

$$H = \sum_{\lambda\lambda'} \int_{-L}^L dx \left[ c_{\lambda}^{\dagger} \left( -\frac{\hbar^2 \partial_x^2}{2m^*} - \mu + h_x \sigma_x + i\alpha \sigma_y \partial_x \right) c_{\lambda'} \right] + \int_{-L}^L dx \left( \Delta c_{\uparrow} c_{\downarrow} + \text{h.c.} \right), \quad (15)$$

where  $\lambda$  is each Nambu term for each lattice site, resulting in  $4N$  different values,  $m^*$  is the effective mass of an electron,  $\mu$  is the chemical potential,  $c^{\dagger}/c$  are creation/annihilation operators,  $\sigma_x$  and  $\sigma_y$  are Pauli matrices acting in spin space,  $\Delta$  is the proximity-induced superconducting pairing potential and  $h_x$  is the Zeeman energy gap proportional to the magnetic field.  $\alpha$  is the spin-orbit coupling strength given by (4).

The tight-binding Hamiltonian can be written as [29]

$$H = \sum_{k=1}^N \left[ -\frac{\mu}{2} (c_{k\uparrow}^{\dagger} c_{k\uparrow} + c_{k\downarrow}^{\dagger} c_{k\downarrow}) + \Delta (c_{k\uparrow}^{\dagger} c_{k\downarrow}^{\dagger} - c_{k\downarrow}^{\dagger} c_{k\uparrow}^{\dagger}) + \frac{h_x}{2} (c_{k\uparrow}^{\dagger} c_{k\downarrow} + c_{k\downarrow}^{\dagger} c_{k\uparrow}) - t (c_{k\uparrow}^{\dagger} c_{k+1\uparrow} + c_{k\downarrow}^{\dagger} c_{k+1\downarrow}) + \alpha (c_{k\uparrow}^{\dagger} c_{k+1\downarrow} - c_{k\downarrow}^{\dagger} c_{k+1\uparrow}) \right] + \text{h.c.}, \quad (16)$$

where  $c_k^{\dagger}/c_k$  are creation/annihilation operators with  $k$  as the lattice index and  $t$  is the hopping integral for the nearest neighbor site on the nanowire. The hopping integral is given by

$$t = \frac{\hbar^2}{2m^*a^2}. \quad (17)$$

The Hamiltonian in (16) was written as a matrix  $H_{ij}$  using the relationship  $H = \frac{1}{2} \vec{\Psi}^{\dagger} H_{ij} \vec{\Psi}$ .

$$\begin{bmatrix} -\mu & h_x & \Delta & 0 & -t & \alpha & & & & & \\ h_x & -\mu & 0 & \Delta & -\alpha & -t & 0 & & & & \\ \Delta & 0 & \mu & h_x & 0 & 0 & t & -\alpha & & & \\ 0 & \Delta & h_x & \mu & 0 & 0 & \alpha & t & \ddots & & \\ \hline -t & -\alpha & 0 & 0 & -\mu & h_x & \Delta & 0 & \ddots & & \\ \alpha & -t & 0 & 0 & h_x & -\mu & 0 & \Delta & \ddots & & \\ & & 0 & t & \alpha & \Delta & 0 & \mu & h_x & \ddots & \\ & & & -\alpha & t & 0 & \Delta & h_x & \mu & \ddots & \\ \hline & & & & \ddots \end{bmatrix} \quad (18)$$

The block off-diagonal terms come from the  $k+1$  indices in the  $t$  and  $\alpha$  terms of the Hamiltonian. These describe the effect that neighboring sites have on each other.

After solving the Schrödinger equation as an eigenvalue problem, the absolute values of the four terms that make

up the Nambu spinor were calculated for each site and then squared in order to receive the probability associated with the wavefunction. The probability for each term to be occupied by the associated particle (electron/hole) was then summed in order to find the occupational probability  $P_k$ , the probability for each site in the lattice to be occupied

$$P_k = |\Psi_{\uparrow k}|^2 + |\Psi_{\downarrow k}|^2 + |\Psi_{\uparrow k}^\dagger|^2 + |\Psi_{\downarrow k}^\dagger|^2. \quad (19)$$

This was then plotted in Fig. 8 and the eigenenergies closest to zero were plotted in Fig. 7.

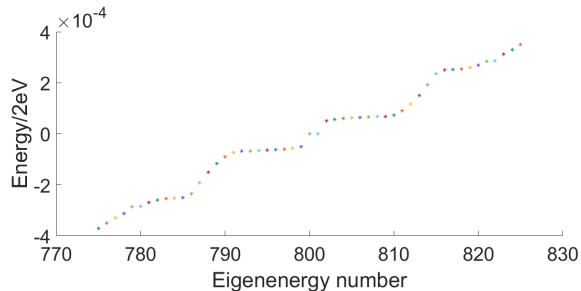


FIG. 7: The eigenenergies in the system. Only the energies closest to zero are included in this plot. Parameter values in Table I.

The topological energy gap can be clearly seen in Fig. 7 as well as the Majorana bound states in the middle of the gap. The topological energy gap is the energy gap between eigenenergies number 799 and 802. The states in the middle of the gap have eigenenergy numbers 800 and 801.

TABLE I: Parameters used in the simple nanowire system

$N$	$\mu/t$	$\Delta/\mu\text{eV}$	$h_x/\mu\text{eV}$	$t/\text{meV}$	$m^*/m_e$	$\alpha_R/\text{p eV}$	$a/\text{nm}$	$L/\mu\text{m}$
400	-2	200	300	66.3	0.023	16	5	2

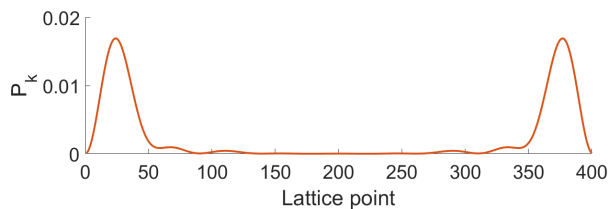


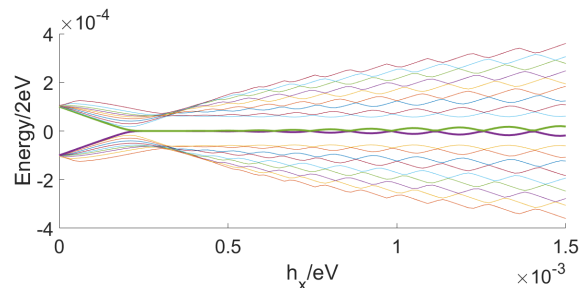
FIG. 8: The occupational probability  $P_k$  of the two states closest to zero energy plotted along the lattice sites. Parameter values in Table I.

Fig. 8 shows that the  $P_k$  of the Majorana bound states are highly localized at the edges of the wire which is characteristic for Majorana bound states as explained in Section II C. There is also no appreciable overlap of the different states at this scale, which is ideal for low decoherence.

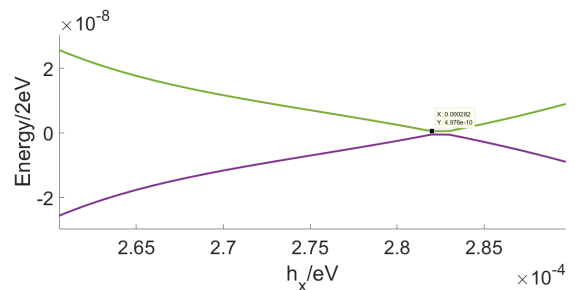
For these plots the parameter values in Table I were used. In order to further study the system, the magnetic field was varied and the eigenenergies were plotted as a function of the magnetic field strength as seen in Fig. 9. The requirement for a topological phase transition (9) as discussed in Section II C is slightly shifted due to defining zero energy as the bottom of the energy band, this will lead to the following change [30]

$$h_x = \sqrt{\Delta^2 + (\mu + 2t)^2} = 200 \mu\text{eV}. \quad (20)$$

It is worth mentioning that a topological phase transition is not possible in a finite system and what is discussed here is merely the closest analogy in a finite system defined as the point where the eigenenergies of the Majorana bound states are closest to zero. Since the eigenenergies will oscillate as a function of  $h_x$ , they will reach a minimum several times. The minimum chosen to represent the topological phase transition in a finite system is the one with the lowest value of  $h_x$ .



(a) Zoomed out.



(b) Zoomed in, the topological phase transition is marked.

FIG. 9: The eigenenergies closest to zero as a function of magnetic field strength. Parameter values in Table I.

In Fig. 9b, the topological phase transition happens at  $h_x = 282 \mu\text{eV}$ , which is larger than the theoretical value of  $200 \mu\text{eV}$ . This is because the theoretical value is based on an infinitely long wire, which is not simulated here. The finite wire will lead to a bending of the line intersecting at 0, seen in Fig. 9a, which in turn leads to a higher value of  $h_x$  at the intersection. After the topological phase transition, the energy gap can be seen growing as a function of  $h_x$ , which is expected due to (8) discussed in Section II C. It will reach a limit however, because eventually the topological energy gap seen in Fig. 4e will



In the same way as in the previous section, the Schrödinger equation was solved and the eigenenergies closest to zero were plotted in Fig. 11 and the occupational probability along the nanowire was plotted in Fig. 12. The values used for the parameters in the plots can be found in Table II where  $W$  is the width of the barrier.

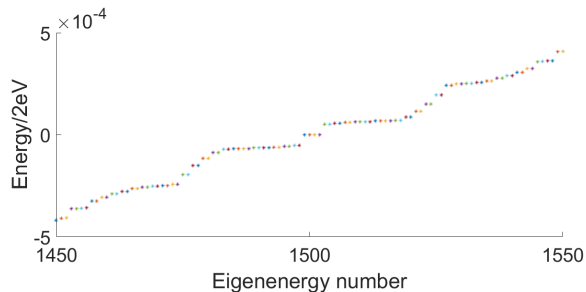


FIG. 11: The eigenenergies in the Josephson junction system. Only the energies closest to zero are included in this plot. Parameter values in Table II.

In Fig. 11 the topological energy gap can once again be clearly seen, however this time there are four bound states in the middle of the gap. These correspond to the four Majorana bound states expected in this system.

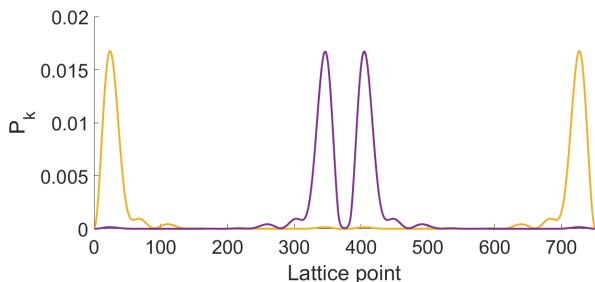
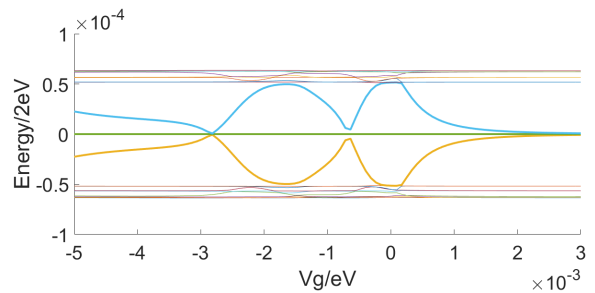
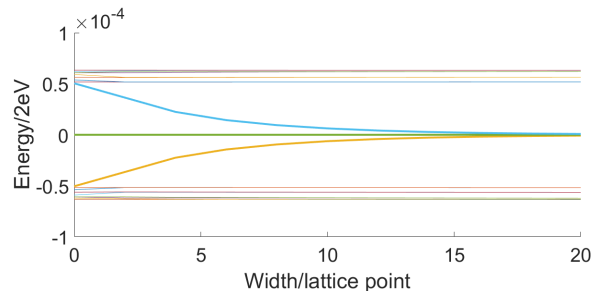


FIG. 12: The occupational probability  $P_k$  of the four states closest to zero energy in the Josephson junction system plotted along the lattice sites. Parameter values in Table II.

In Fig. 12 the  $P_k$  of the Majorana bound states are once again located at the edges, but in this system there are additional spikes at the edges of the Josephson barrier. These correspond to the added Majorana bound states in this system.



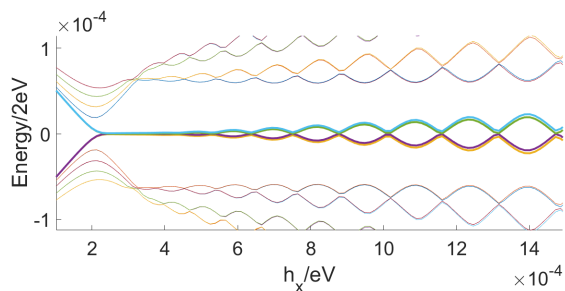
(a) Height.



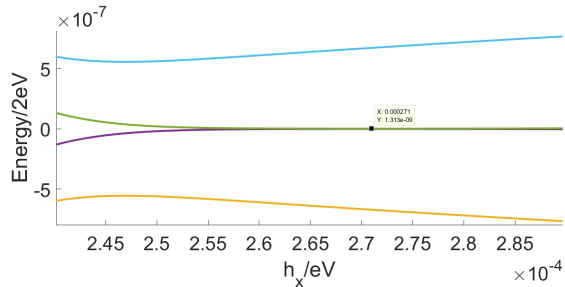
(b) Width.

FIG. 13: The eigenenergies closest to zero as a function of the barrier height and width. The height plot has negative values included, which corresponds to replacing the potential barrier with a potential well. Parameter values in Table II.

To further investigate the impact of the potential barrier, the eigenenergies closest to zero were plotted as a function of the barrier's height and width in Fig. 13. As the height and/or width increases, it changes the topological energy gap from the original two Majorana state system into a four Majorana state system by binding two more energy states to zero energy.



(a) Zoomed out.



(b) Zoomed in, the topological phase transition is marked.

FIG. 14: The eigenenergies closest to zero in the Josephson junction system as a function of magnetic field strength. Parameter values in Table II.

In the same way as with the previous system, the magnetic field's impact on the eigenenergies was investigated and can be seen in Fig. 14. Once again there are oscillations of the eigenenergies at higher values of  $h_x$  in Fig. 14a. The topological phase transition is marked in Fig. 14b as the two eigenenergies closest to zero intersect at zero energy.

In Section IID the terms  $E_0$  and  $E_M$  were introduced in (11) and (12). The values of these are results of the diagonalization and can be seen in Fig. 14b as the separation of the states from zero energy. The two Majorana bound states closest to the Josephson junction will never fully reach zero energy because of the existence of the  $E_M$  term. It is the  $E_M$  term that pushes the energy of the two states from zero and not the  $E_0$  term because there are still two states near zero energy. If  $E_0$  was larger than  $E_M$ , all of the states would be pushed from zero energy as  $E_0$  affects both the edge states and the states near the Josephson junction.

The topological phase transition can be seen at  $h_x = 271 \mu\text{eV}$ . Adding a barrier will not affect the requirement for the topological phase transition in any significant way as it is a bulk effect and the barrier is not part of the bulk. However, the total wire is longer in this case compared to the previous case, which means that if the barrier does not adequately divide the system into two topologically separate parts, a value closer to the infinite case is expected which could be what is seen here.

#### IV. MULTI-BAND MODEL

In order to more realistically model the nanowire, a two- and three-band model was created. This models a wire with width  $L_y$ , where  $L_x \gg L_y \gg L_z$ . The different energy bands will be separated by the band splitting energy  $E_{sb}$  and they will interact with each other due to the band mixing energy  $E_{bm}$  and multi-band proximity-induced superconductivity  $\Delta_{ij}$  where  $i, j$  denote the dif-

ferent bands.  $E_{sb}$  comes from a confinement effect due to the finite width of the wire.  $E_{bm}$  comes from a first order perturbation of the spin-orbit term.

As mentioned in Section II C, Majorana bound states are only possible when an odd number of Zeeman-split energy subbands are occupied. This will limit the range of possible values of  $\mu$  in order to find Majorana bound states in the system and  $E_{sb}$  will separate the possible ranges, see Fig. 15.

$$\left[ \begin{array}{cccc|cccc} -\mu + \frac{\hbar^2 k^2}{2m^*} & h_x + i\alpha_R k & \Delta_{11} & 0 & 0 & iE_{bm} & \Delta_{12} & 0 \\ h_x - i\alpha_R k & -\mu + \frac{\hbar^2 k^2}{2m^*} & 0 & \Delta_{11} & iE_{bm} & 0 & 0 & \Delta_{12} \\ \Delta_{11} & 0 & \mu - \frac{\hbar^2 k^2}{2m^*} & h_x + i\alpha_R k & \Delta_{12} & 0 & 0 & iE_{bm} \\ 0 & \Delta_{11} & h_x - i\alpha_R k & \mu - \frac{\hbar^2 k^2}{2m^*} & 0 & \Delta_{12} & iE_{bm} & 0 \\ \hline 0 & -iE_{bm} & \Delta_{12} & 0 & -\mu + 3E_{sb} + \frac{\hbar^2 k^2}{2m^*} & h_x + i\alpha_R k & \Delta_{22} & 0 \\ -iE_{bm} & 0 & 0 & \Delta_{12} & h_x - i\alpha_R k & -\mu + 3E_{sb} + \frac{\hbar^2 k^2}{2m^*} & 0 & \Delta_{22} \\ \Delta_{12} & 0 & 0 & -iE_{bm} & \Delta_{22} & 0 & \mu - 3E_{sb} - \frac{\hbar^2 k^2}{2m^*} & h_x + i\alpha_R k \\ 0 & \Delta_{12} & -iE_{bm} & 0 & 0 & \Delta_{22} & h_x - i\alpha_R k & \mu - 3E_{sb} - \frac{\hbar^2 k^2}{2m^*} \end{array} \right] \quad (22)$$

##### A. Two-Band Model

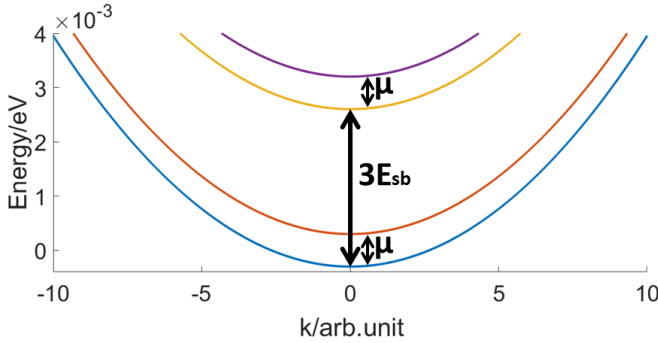


FIG. 15: Calculated energy bands of the two-band model.  $E_{sb}$  is marked in the plot as well as the range of  $\mu$  where only one Zeeman split subband is occupied. This plot has been calculated by diagonalizing (22).

Parameter values in Table III except  $\mu = \Delta_{11} = \Delta_{12} = \Delta_{22} = \alpha_R = 0$ .

The energy bands of the two-band model are shown in Fig. 15. This was calculated using a Fourier transform of (23) to get (22) in order to calculate the band structure in the case of an infinitely long wire in the same way as in Section II C. The Hamiltonian describing the system can be expressed as [28, 30]

$$\begin{aligned} H = & \sum_{\lambda\lambda'} \int_{-L}^L dx \left[ c_{\lambda}^{\dagger} \left( -\frac{\hbar^2 \partial_x^2}{2m^*} - \mu + h_x \sigma_x + i\alpha \sigma_y \partial_x \right) c_{\lambda} \right. \\ & + d_{\lambda}^{\dagger} \left( -\frac{\hbar^2 \partial_x^2}{2m^*} - \mu + 3E_{sb} + h_x \sigma_x + i\alpha \sigma_y \partial_x \right) d_{\lambda} \\ & \left. + E_{bm} \left( c_{\lambda}^{\dagger} (i\sigma_x) d_{\lambda'} - d_{\lambda}^{\dagger} (i\sigma_x) c_{\lambda'} \right) \right] \\ & + \int_{-L}^L dx \left[ \Delta_{11} c_{\uparrow}^{\dagger} c_{\downarrow}^{\dagger} + \Delta_{22} d_{\uparrow}^{\dagger} d_{\downarrow}^{\dagger} \right. \\ & \left. + \Delta_{12} \left( d_{\uparrow}^{\dagger} c_{\downarrow}^{\dagger} + c_{\uparrow}^{\dagger} d_{\downarrow}^{\dagger} \right) + \text{h.c.} \right] \end{aligned} \quad (23)$$

where  $d^{\dagger}/d$  are creation/annihilation operators for the second band,  $E_{sb}$  is the band splitting energy given by

$$E_{sb} = \frac{\hbar^2 \pi^2}{2m^* L_y^2}, \quad (24)$$

the factor 3 before  $E_{sb}$  is given by  $2^2 - 1^2$  and  $E_{bm}$  is the band mixing energy given by

$$\begin{aligned} E_{bm} = & \int_0^{L_y} dy \frac{2\alpha_R}{L_y} \sin \frac{n_y \pi y}{L_y} \partial_y \sin \frac{n'_y \pi y}{L_y} = \\ & [n_y = 1, n'_y = 2] = \frac{8\alpha_R}{3L_y}. \end{aligned} \quad (25)$$

$\Delta_{11}$  is the proximity-induced superconducting pairing potential in band 1,  $\Delta_{22}$  is the equivalent in band 2 and  $\Delta_{12}$  is the induced superconductivity between the different bands. When calculating  $E_{bm}$  the value of  $\alpha_R = 8$  peV was used.

TABLE III: Parameters used in the two-band model

$N$	$\mu/t$	$\Delta_{11}/\mu\text{eV}$	$\Delta_{22}/\mu\text{eV}$	$\Delta_{12}/\mu\text{eV}$	$h_x/\mu\text{eV}$	$m^*/m_e$	$\alpha_R/\text{peV}$	$a/\text{nm}$	$L_x/\mu\text{m}$	$L_y/\text{nm}$	$t/\text{meV}$	$E_{sb}/\mu\text{eV}$
400	-2	200	200	100	300	0.023	16	5	2	130	66.3	967

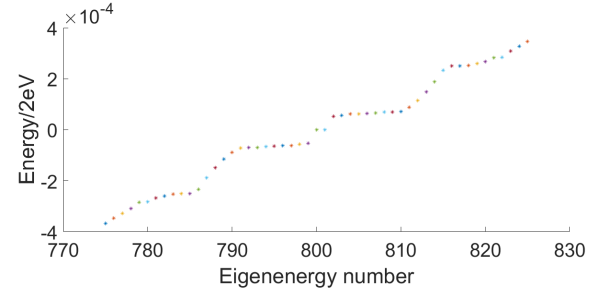
The Hamiltonian was discretized in the same way as in earlier sections, except that the additional band meant that each lattice point was represented by an  $8 \times 8$  matrix (26) instead of a  $4 \times 4$  matrix. The first quadrant is the same as earlier, which now represents the first band, the two off-diagonal quadrants have the inter-band terms and the last quadrant has the band 2 terms. The off-diagonal terms that stem from the  $t$  and  $\alpha$  terms of the Hamiltonian will remain just as in earlier cases and look the same for band 2, but are not shown explicitly in (26).

The same eigenvalue problem was solved as in earlier sections, however this time the calculated eigenenergies and  $P_k$ -functions were allocated to the two different energy bands. The separation was done by allocating a weight to each band corresponding to the sum of the occupational probability in each lattice site for that band. The states were then sorted into the band where it had the largest weight. The states will always have some weight in both bands, but this separation was made to more clearly illustrate some important properties of the system.

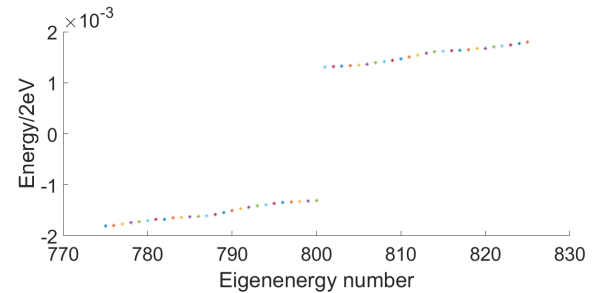
$$\left[ \begin{array}{cccc|cccc}
 -\mu & h_x & \Delta_{11} & 0 & 0 & iE_{bm} & \Delta_{12} & 0 \\
 h_x & -\mu & 0 & \Delta_{11} & iE_{bm} & 0 & 0 & \Delta_{12} \\
 \Delta_{11} & 0 & \mu & h_x & \Delta_{12} & 0 & 0 & iE_{bm} \\
 0 & \Delta_{11} & h_x & \mu & 0 & \Delta_{12} & iE_{bm} & 0 \\
 \hline
 0 & -iE_{bm} & \Delta_{12} & 0 & -\mu + 3E_{sb} & h_x & \Delta_{22} & 0 \\
 -iE_{bm} & 0 & 0 & \Delta_{12} & h_x & -\mu + 3E_{sb} & 0 & \Delta_{22} \\
 \Delta_{12} & 0 & 0 & -iE_{bm} & \Delta_{22} & 0 & \mu - 3E_{sb} & h_x \\
 0 & \Delta_{12} & -iE_{bm} & 0 & 0 & \Delta_{22} & h_x & \mu - 3E_{sb}
 \end{array} \right] \quad (26)$$

In the following plots, the system was investigated both with and without any band interaction terms,  $E_{bm} = 0$  and  $\Delta_{12} = 0$ . Unless otherwise specified, all the parameters used are given by Table III, which means that the chemical potential is set to the bottom of band 1.

The eigenenergies for both bands were plotted with the interaction terms in Fig. 16. Half of the eigenenergies will be weighted to band 1 and half to band 2. The topological energy gap can be clearly seen in Fig. 16a with Majorana bound states in the middle, while in Fig. 16b there are no Majorana bound states, leading to a topological energy gap in band 2 without any states in the middle. This means that the Majorana bound states are located in band 1, which is expected since the chemical potential has been set to the bottom of band 1.



(a) Band 1.



(b) Band 2.

FIG. 16: The eigenenergies closest to zero in the different bands with band interaction terms. Parameter values in Table III.

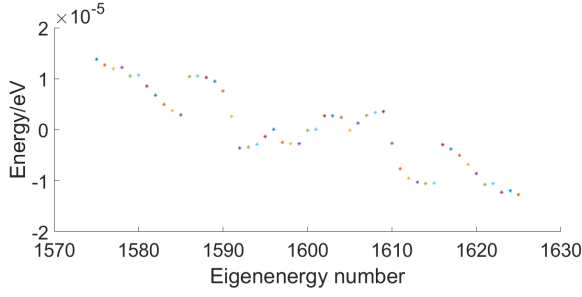


FIG. 17: The difference between the eigenenergies closest to zero with and without band interaction terms. Parameter values in Table III.

In Fig. 17 the difference between the eigenenergies closest to zero with ( $E_{ig}$ ) and without ( $E_{ig_0}$ ) band interaction terms ( $E_{ig} - E_{ig_0}$ ) is plotted. In this plot all of the eigenenergies are considered, however, only the ones closest to zero are plotted. The shifts in energy are one order of magnitude smaller than the energies in Fig. 16a and are anti-symmetric around the middle eigenenergy number.

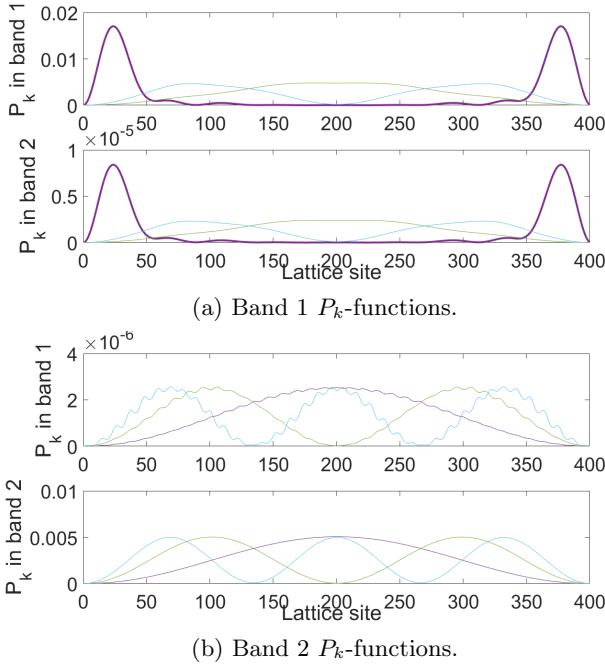


FIG. 18: The occupational probability  $P_k$  of the six states closest to zero energy in the different bands with band interaction. Parameter values in Table III.

There is a clear difference in the occupational probability  $P_k$  along the nanowire with and without band interaction, which can be seen in Fig. 18 and Fig. 19, respectively. In each band plot, the  $P_k$ -functions corresponding to the six eigenenergies closest to zero for that band were plotted, one plot for their representation in each band. This means that e.g. Fig. 18a has the six  $P_k$ -functions that have energies closest to zero in band 1,

the top plot shows the part of these functions that corresponds to band 1 and the bottom plot shows the part of these functions that corresponds to band 2. Fig 18b is structured the same way, this is why the top plot has the highest amplitude in Fig. 18a while the bottom plot has the highest amplitude for Fig 18b, as the  $P_k$ -functions plotted are the ones with highest probability to be occupied in those bands. The bottom plot in Fig. 18a looks similar to the top plot, but has a lower amplitude. The same behavior is observed in Fig. 18b but here the bottom plot has a higher amplitude. The  $P_k$ -functions in the top plot in Fig. 18b oscillate due to a high momentum in band 1, but retains the envelope function from band 2. This is a result of having to maintain the same energy in band 1 as in band 2, corresponding to a horizontal shift in Fig. 15.

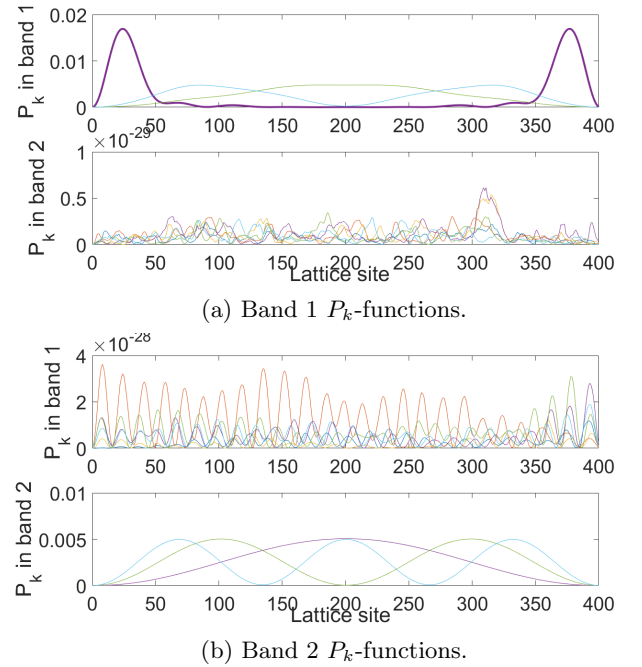
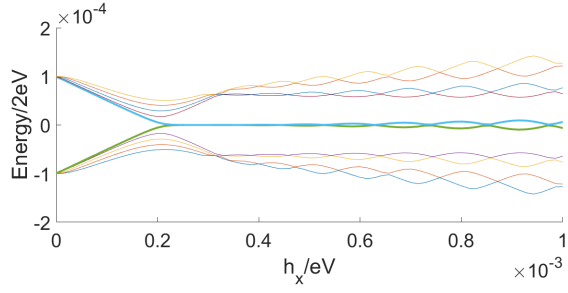
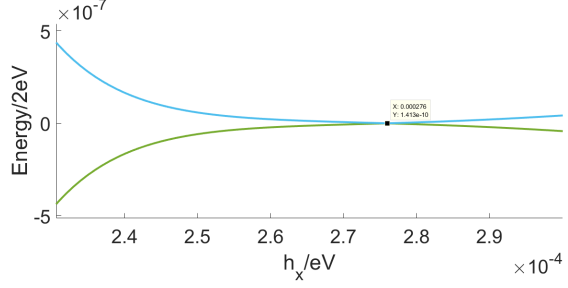


FIG. 19: The occupational probability  $P_k$  of the six states closest to zero energy in the different bands without band interaction,  $E_{bm} = 0$  and  $\Delta_{12} = 0$ . Parameter values in Table III.

The occupational probability  $P_k$  without band interaction terms is plotted in Fig. 19. In the band with lower amplitude in Fig. 19, the amplitude is so low that  $P_k$  can be approximated to zero for all lattice sites and the results are simply numerical errors. This is expected as without band interaction, the  $P_k$ -functions will not be able to span across both bands.

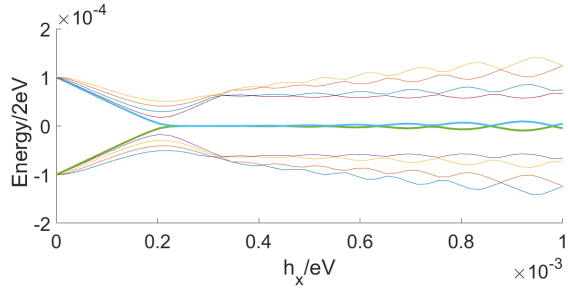


(a) Zoomed out.

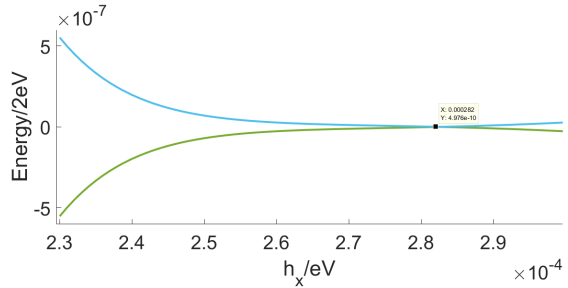


(b) Zoomed in, the topological phase transition is marked.

FIG. 20: The eigenenergies closest to zero as a function of magnetic field strength with band interaction. Parameter values in Table III.



(a) Zoomed out.



(b) Zoomed in, the topological phase transition is marked.

FIG. 21: The eigenenergies closest to zero as a function of magnetic field strength without band interaction,  $E_{bm} = 0$  and  $\Delta_{12} = 0$ . Parameter values in Table III.

The eigenenergies closest to zero as a function of  $h_x$  are shown in Fig. 20 and Fig. 21. There is no noticeable difference in the general shape of the eigenenergies as a function of  $h_x$  with and without band interaction for these values of  $E_{bm}$  and  $\Delta_{12}$ . However the topological phase transition occurs at  $h_x = 276 \mu\text{eV}$  and  $h_x = 282 \mu\text{eV}$  with and without band interaction, respectively. This means that band interaction will lower the transition point.

In order to determine how much impact each of the band interaction terms have on the topological phase transition, the value of  $h_x$  at the topological phase transition was plotted as a function of  $\Delta_{12}$  for two different values of  $E_{bm}$  in Fig. 22. A clear, non-linear dependence on  $\Delta_{12}$  can be seen in both Fig. 22a & Fig. 22b and it also behaves slightly differently with and without the  $E_{bm}$  term. From these results it appears that the parameter choices of  $\Delta_{12} = 0$  and  $E_{bm} \neq 0$  would minimize the value of  $h_x$  where the topological phase transition occurs.

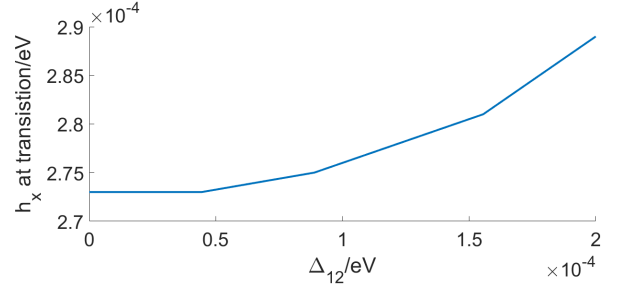
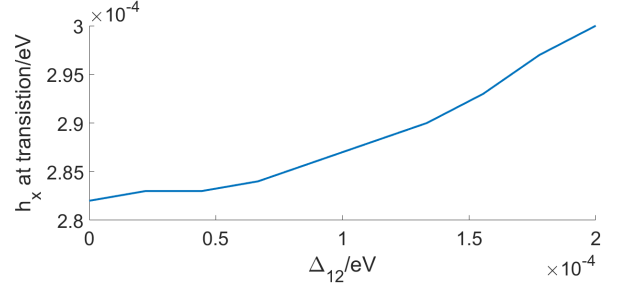
(a) With band interaction,  $E_{bm} \neq 0$ .(b) Without band interaction,  $E_{bm} = 0$ .

FIG. 22:  $h_x$  where the topological phase transition occurs as a function of  $\Delta_{12}$ . Parameter values in Table III.

Next I study how  $L_y$  affects the eigenenergies. This has been plotted for each separate band in Fig. 23. Band 1 is not affected much by  $L_y$  as seen in Fig. 23a except for a minimum at  $L_y = 350$  nm seen in Fig. 23b, however, the energy shift for the states in band 2 from zero energy is getting smaller as  $L_y$  is increased, as seen in Fig. 23c. This is due to the inverse quadratic dependence of  $L_y$  for  $E_{sb}$ , see (24), meaning that as  $L_y$  is increased, the eigenenergies closest to zero in band 2 will decrease in energy until they reach a minimum defined by the topological energy gap. The excited states in Fig. 23a sharply change energy at higher values of  $L_y$ , however this could be due to numerical errors as there were not enough data points simulated for  $L_y$  as can be seen in the jagged curve in Fig. 23c. It can also be due to the fact that for large values of  $L_y$  the system is no longer well modelled as 1D.

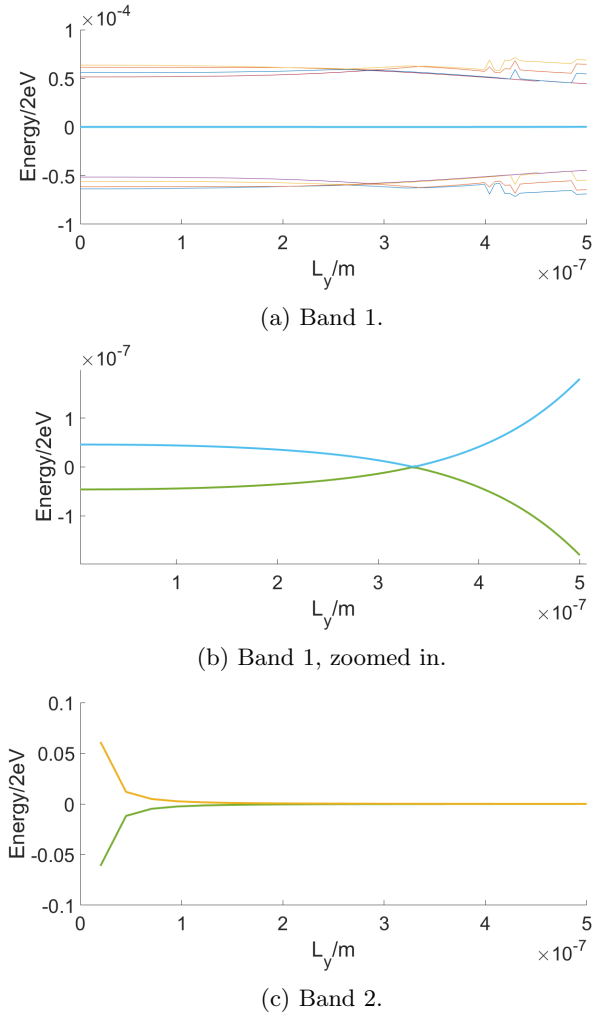


FIG. 23: The eigenenergies closest to zero as a function of  $L_y$  for each band with band interaction. Parameter values in Table III.

As the two energy bands will lead to Majorana bound states being able to exist at the bottom of two different bands depending on  $\mu$ , it is valuable to see how the

eigenenergies are affected as  $\mu$  is changed, this is therefore plotted for each band in Fig. 24. As  $\mu$  is increased, eventually the second Zeeman split subband will be reached and a split in energy will happen, see Fig. 24a. Once  $\mu$  reaches the second band at around  $-0.1324$  eV, the lowest Zeeman split subband will be reached leading to a zero energy state seen in Fig. 24b. As  $\mu$  is increased further, once again the second Zeeman split subband will be reached and the Majorana bound states will disappear.

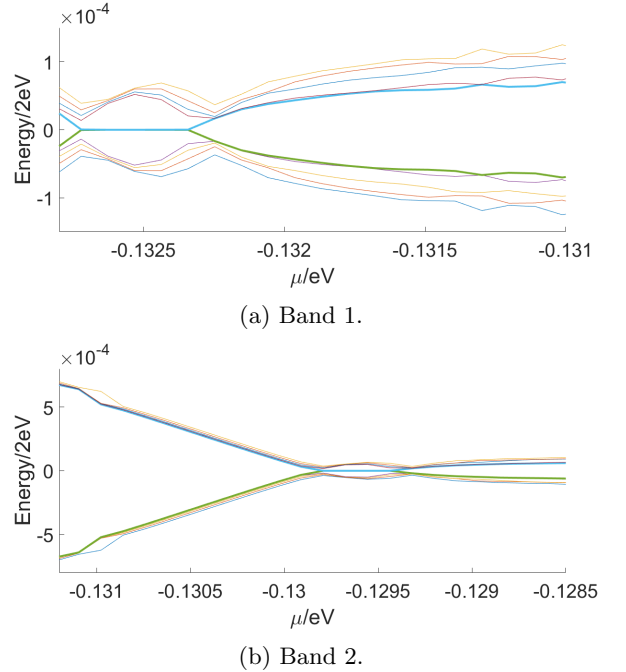


FIG. 24: The lowest eigenenergies as a function of  $\mu$  for each different band with band interaction. Note that the scales on the y-axes are different for the different subfigures. Parameter values in Table III.

In order to understand the topological transformation that happens when the first Zeeman split subband in band 2 is reached, the eigenenergies and  $P_k$ -function were plotted for  $\mu$  the bottom of band 2,  $\mu = -2t + 3E_{sb}$ .

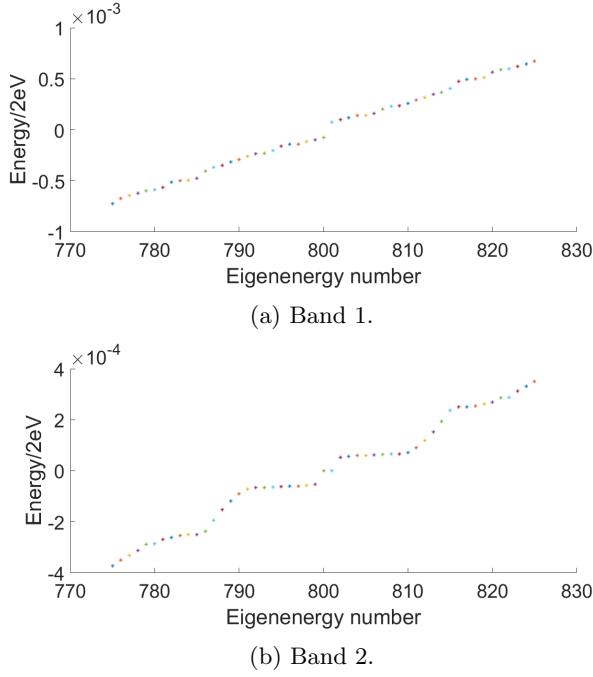


FIG. 25: The eigenenergies closest to zero in the different bands with band interaction terms when  $\mu = -2t + 3E_{sb}$ . Other parameter values in Table III.

In Fig. 25 it can be seen that the Majorana bound states have moved to band 2 for this value of  $\mu$ .

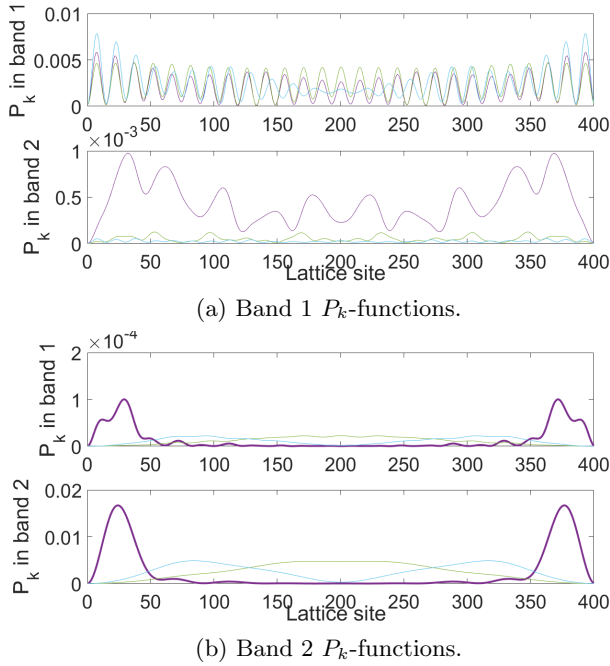


FIG. 26: The occupational probability  $P_k$  of the six states closest to zero energy in the different bands with band interaction when  $\mu = -2t + 3E_{sb}$ . Other parameter values in Table III.

As can be seen in Fig. 26, the Majorana bound states will have the largest weight in band 2 instead of band 1 for this value of  $\mu$ .

## B. Three-Band Model

A third band was added to the model in order to verify that the observations found in the 2-band system, such as a lower occupational probability for higher energy bands, were not specific to that system and were in fact indicative of a general multi-band system.

The Hamiltonian describing the system can be expressed as

$$\begin{aligned}
 H = & \sum_{\lambda\lambda'} \int_{-L}^L dx \left[ c_{\lambda}^{\dagger} \left( -\frac{\hbar^2 \partial_x^2}{2m^*} - \mu + h_x \sigma_x + i\alpha \sigma_y \partial_x \right) c_{\lambda'} \right. \\
 & + d_{\lambda}^{\dagger} \left( -\frac{\hbar^2 \partial_x^2}{2m^*} - \mu + 3E_{sb} + h_x \sigma_x + i\alpha \sigma_y \partial_x \right) d_{\lambda'} \\
 & + e_{\lambda}^{\dagger} \left( -\frac{\hbar^2 \partial_x^2}{2m^*} - \mu + 8E_{sb} + h_x \sigma_x + i\alpha \sigma_y \partial_x \right) e_{\lambda'} \\
 & + E_{bm12} \left( c_{\lambda}^{\dagger} (i\sigma_x) d_{\lambda'} - d_{\lambda}^{\dagger} (i\sigma_x) c_{\lambda'} \right) \\
 & \left. + E_{bm23} \left( d_{\lambda}^{\dagger} (i\sigma_x) e_{\lambda'} - e_{\lambda}^{\dagger} (i\sigma_x) d_{\lambda'} \right) \right] \\
 & + \int_{-L}^L dx \left[ \Delta_{11} c_{\uparrow}^{\dagger} c_{\downarrow}^{\dagger} + \Delta_{22} d_{\uparrow}^{\dagger} d_{\downarrow}^{\dagger} + \Delta_{33} e_{\uparrow}^{\dagger} e_{\downarrow}^{\dagger} \right. \\
 & + \Delta_{12} \left( d_{\uparrow}^{\dagger} c_{\downarrow}^{\dagger} + c_{\uparrow}^{\dagger} d_{\downarrow}^{\dagger} \right) + \Delta_{23} \left( e_{\uparrow}^{\dagger} d_{\downarrow}^{\dagger} + d_{\uparrow}^{\dagger} e_{\downarrow}^{\dagger} \right) \\
 & \left. + \Delta_{13} \left( e_{\uparrow}^{\dagger} c_{\downarrow}^{\dagger} + c_{\uparrow}^{\dagger} e_{\downarrow}^{\dagger} \right) + \text{h.c.} \right]
 \end{aligned} \tag{27}$$

where  $e^{\dagger}/e$  are creation/annihilation operators for the third band,  $E_{bm12} = \frac{8\alpha_R}{3L_y}$  is the band mixing energy between the first and second band, as seen in (25) and  $E_{bm23} = \frac{24\alpha_R}{5L_y}$  is the band mixing energy between the second and third band. When calculating both  $E_{bm12}$  and  $E_{bm23}$  the value of  $\alpha_R = 8$  peV was used.

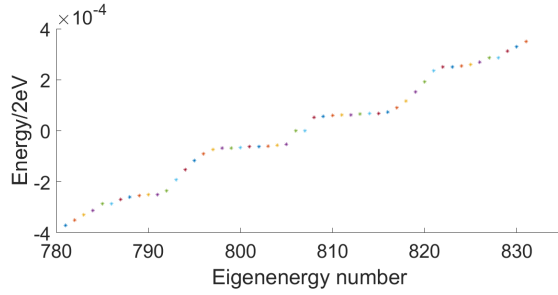
The Hamiltonian was discretized in the same way as in earlier sections, however the third band gives rise to a  $12 \times 12$  matrix for each lattice point.

TABLE IV: Parameters used in the three-band model

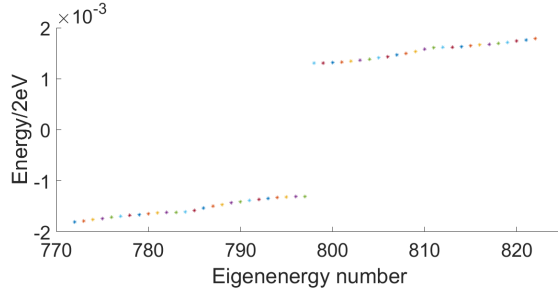
$N$	$\mu/t$	$\Delta_{11}/\mu\text{eV}$	$\Delta_{22}/\mu\text{eV}$	$\Delta_{33}/\mu\text{eV}$	$\Delta_{12}/\mu\text{eV}$	$\Delta_{23}/\mu\text{eV}$	$\Delta_{13}/\mu\text{eV}$	$h_x/\mu\text{eV}$	$m^*/m_e$	$\alpha_R/\text{peV}$	$a/\text{nm}$	$L_x/\mu\text{m}$	$L_y/\text{nm}$	$t/\text{meV}$	$E_{sb}/\mu\text{eV}$
400	-2	200	200	200	100	100	100	300	0.023	16	5	2	130	66.3	967

$-\mu$	$h_x$	$\Delta_{11}$	0	0	$iE_{bm12}$	$\Delta_{12}$	0	0	0	0	0	$\Delta_{13}$	0
$h_x$	$-\mu$	0	$\Delta_{11}$	$iE_{bm12}$	0	0	$\Delta_{12}$	0	0	0	0	0	$\Delta_{13}$
$\Delta_{11}$	0	$\mu$	$h_x$	$\Delta_{12}$	0	0	$iE_{bm12}$	$iE_{bm12}$	$\Delta_{13}$	0	0	0	0
0	$\Delta_{11}$	$h_x$	$\mu$	0	$\Delta_{12}$	$iE_{bm12}$	0	0	0	$\Delta_{13}$	$\Delta_{13}$	0	0
0	$-iE_{bm12}$	$\Delta_{12}$	0	$-\mu + 3E_{sb}$	$h_x$	$\Delta_{22}$	0	0	0	$iE_{bm23}$	$\Delta_{23}$	0	0
$-iE_{bm12}$	0	0	$\Delta_{12}$	$h_x$	$-\mu + 3E_{sb}$	0	$\Delta_{22}$	$iE_{bm23}$	0	0	0	$\Delta_{23}$	$\Delta_{23}$
$\Delta_{12}$	0	0	$-iE_{bm12}$	$\Delta_{22}$	0	$\mu - 3E_{sb}$	$h_x$	$\Delta_{23}$	0	0	0	$iE_{bm23}$	$iE_{bm23}$
0	$\Delta_{12}$	$-iE_{bm12}$	0	0	$\Delta_{22}$	$h_x$	$\mu - 3E_{sb}$	0	$\Delta_{23}$	$\Delta_{23}$	$iE_{bm23}$	0	0
0	0	$\Delta_{13}$	0	0	$-iE_{bm23}$	$\Delta_{23}$	0	$-\mu + 8E_{sb}$	$h_x$	$\Delta_{33}$	0	0	0
0	0	0	$\Delta_{13}$	$-iE_{bm23}$	0	0	$\Delta_{23}$	$h_x$	$-\mu + 8E_{sb}$	0	$\Delta_{33}$	0	$\Delta_{33}$
$\Delta_{13}$	0	0	0	$\Delta_{23}$	0	0	$-iE_{bm23}$	$\Delta_{33}$	0	$\mu - 8E_{sb}$	$h_x$	$\mu - 8E_{sb}$	$h_x$
0	$\Delta_{13}$	0	0	0	$\Delta_{23}$	$-iE_{bm23}$	0	0	$\Delta_{33}$	$h_x$	$\mu - 8E_{sb}$	0	$\mu - 8E_{sb}$

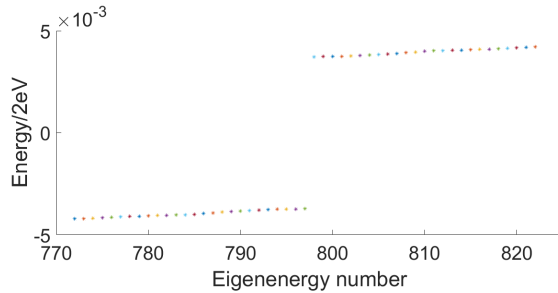
(28)



(a) Band 1.



(b) Band 2.



(c) Band 3.

FIG. 27: The eigenenergies closest to zero in the different bands. Parameter values in Table IV.

The parameters used are given by Table IV. In the same way as earlier, the eigenenergies were plotted in Fig. 27. The topological energy gap can be clearly seen in

Fig. 27a with Majorana bound states in the middle, while Fig. 27b and Fig. 27c do not have any Majorana bound states, which is expected since the chemical potential has been set to the bottom of band 1. As expected, there are still an equal number of eigenenergies in all of the bands and only band 1 has zero-energy states.

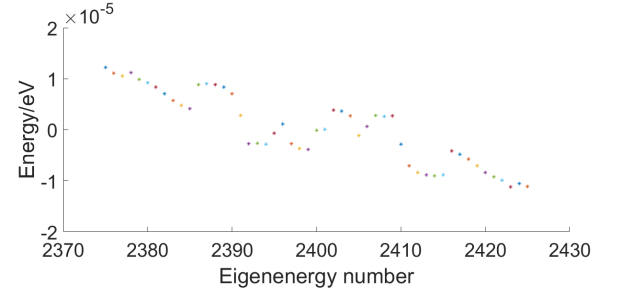


FIG. 28: The difference between the eigenenergies closest to zero with and without band interaction terms. Parameter values in Table IV.

In Fig. 28 the difference between the eigenenergies closest to zero with ( $E_{ig}$ ) and without ( $E_{ig_0}$ ) band interaction terms ( $E_{ig} - E_{ig_0}$ ) is plotted. In this plot all of the eigenenergies are considered, however, only the ones closest to zero are plotted. The shifts in energy are one order of magnitude smaller than the energies in Fig. 27a and are anti-symmetric around the middle eigenenergy number. With the band interaction terms, the eigenenergies are no longer equally distributed in each energy band.

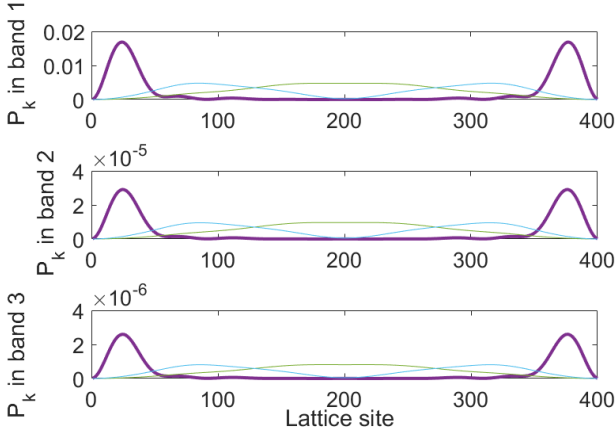
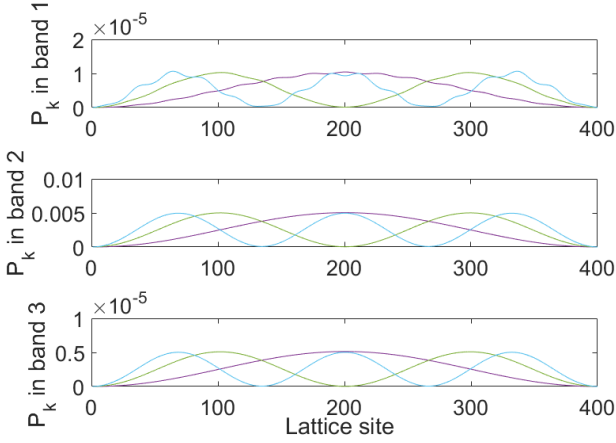
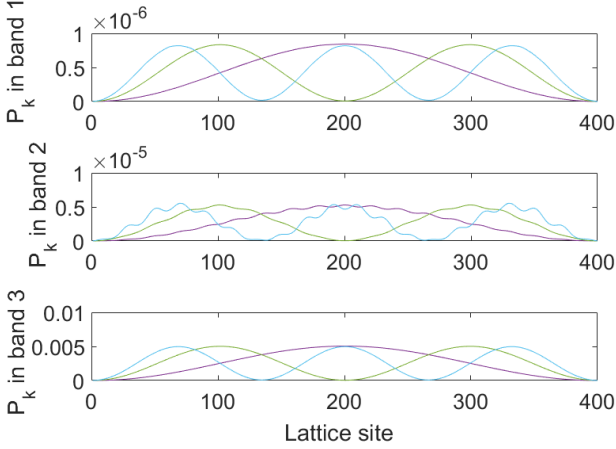
(a) Band 1  $P_k$ -functions.(b) Band 2  $P_k$ -functions.(c) Band 3  $P_k$ -functions.

FIG. 29: The occupational probability  $P_k$  of the six states closest to zero energy in the different bands with band interaction. Parameter values in Table IV.

The occupational probability was also plotted with and without band interaction terms in Fig. 29 and Fig. 30, respectively. The bottom plots in Fig. 29a are similar to the top plot, but with lower amplitude. The same behavior is present in Fig. 29b and Fig. 29c, but with different plots having higher amplitude as the  $P_k$ -function plotted are sorted by which band they have the highest probability to be occupied in. The  $P_k$ -functions in the top plot in Fig. 29b and the middle plot in Fig. 29c oscillate due to these states having a large momentum. As mentioned in Section IV A, this increase in momentum comes from having to maintain the same energy along the different energy bands.

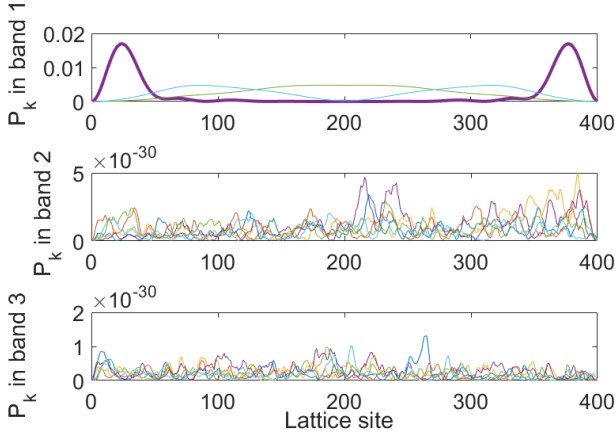
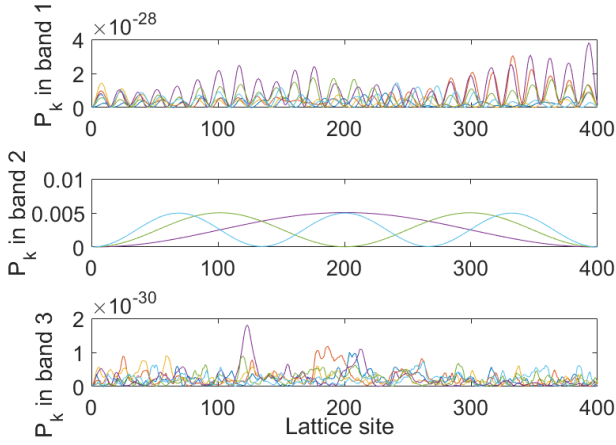
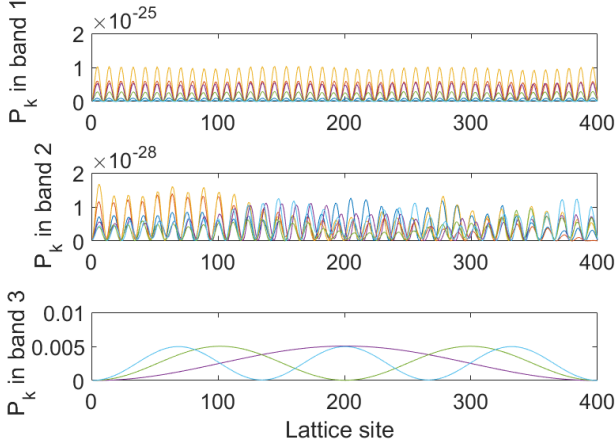
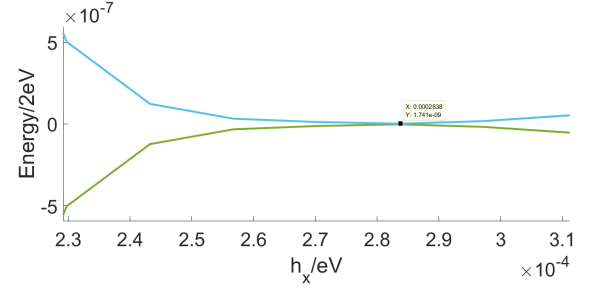
(a) Band 1  $P_k$ -functions.(b) Band 2  $P_k$ -functions.(c) Band 3  $P_k$ -functions.

FIG. 30: The occupational probability  $P_k$  of the six states closest to zero energy in the different bands without band interaction,  $E_{bm} = 0$  and  $\Delta_{12} = \Delta_{23} = \Delta_{13} = 0$ . Parameter values in Table IV.

The occupational probability  $P_k$  without band interaction terms ( $E_{bm} = 0$  and  $\Delta_{12} = \Delta_{23} = \Delta_{13} = 0$ ) is plotted in Fig. 30. Once again,  $P_k$  has a non-zero value in one band at a time, due to the removal of the band interaction. The band 1 and 2  $P_k$ -functions are very similar to the ones in the 2-band case, so the addition of the third band does not seem to noticeably change the system in regards to these elementary investigations, when only looking at the eigenenergies and  $P_k$  and when  $\mu$  is at the bottom of band 1.

Next the topological phase transition's dependence on the band interaction terms was investigated in Fig. 31. For Fig. 31a, the topological transition happens at  $h_x = 284 \mu\text{eV}$  and for Fig. 31b, the transition happens at  $h_x = 283 \mu\text{eV}$ . This is a negligible difference, unlike the one observed in the two-band model. The reason for this difference is unknown for the author of this thesis, however the definition for a topological phase transition in a finite wire explained in Section III A may not truly respect the actual physics.



(a) With interaction.

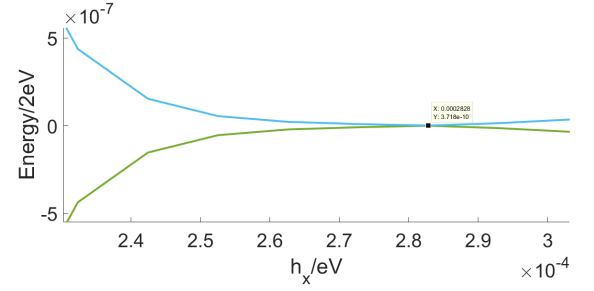
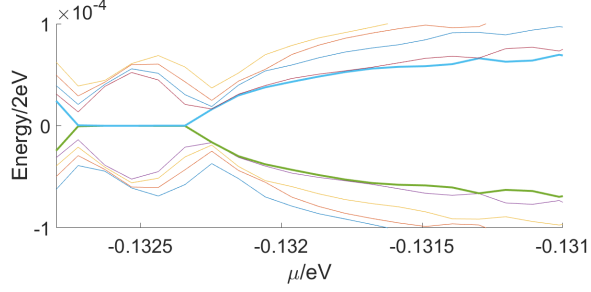
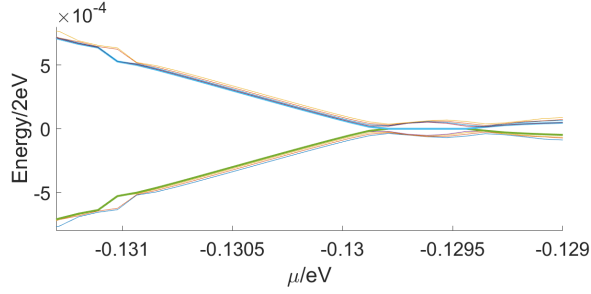
(b) Without interaction,  $E_{bm} = 0$  and  $\Delta_{12} = \Delta_{23} = \Delta_{13} = 0$ .

FIG. 31: The eigenenergies closest to zero as a function of magnetic field strength, zoomed in. Parameter values in Table IV.

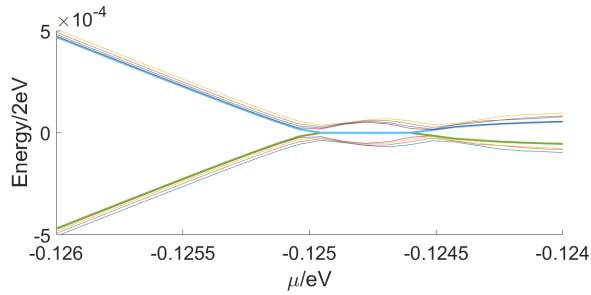
The last thing that needs to be checked is if the behavior of the eigenenergies as a function of  $\mu$  hinted at in Section IV A is repeated in the three-band system. Therefore the eigenenergies as a function of  $\mu$  is plotted in Fig. 32. The zero energy states appearing in different bands for different values of  $mu$  that was seen in the 2 band case is shown here, leading to the conclusion that this behavior will happen independently of the number of energy bands. In a real system there will be an infinite number of bands, leading to a state that will continuously move between allowing Majorana bound states and not as a function of  $\mu$ .



(a) Band 1.



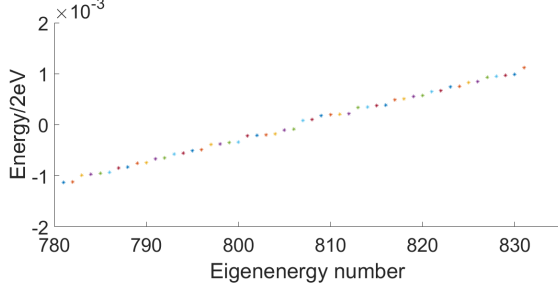
(b) Band 2.



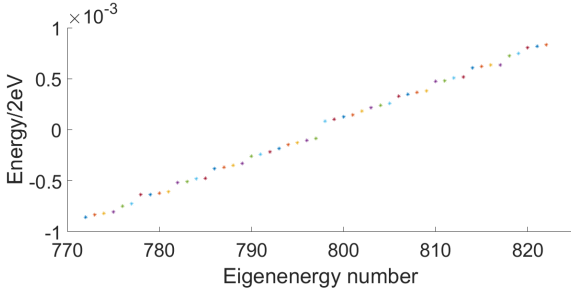
(c) Band 3.

FIG. 32: The eigenenergies closest to zero as a function of  $\mu$  for each band. Note that the scales on the y-axes are different for the different subfigures. Parameter values in Table IV.

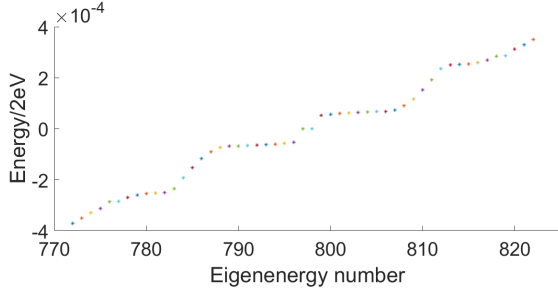
Finally, the eigenenergies and  $P_k$ -functions of the three-band model when  $\mu = -2t + 8E_{sb}$ , i.e. at the bottom of band 3, were plotted in Fig. 33 and Fig. 34. From both figures it is clear that the Majorana bound states have been shifted to band 3.



(a) Band 1.



(b) Band 2.



(c) Band 3.

FIG. 33: The eigenenergies closest to zero in the different bands with band interaction terms when  $\mu = -2t + 8E_{sb}$ . Other parameter values in Table IV.

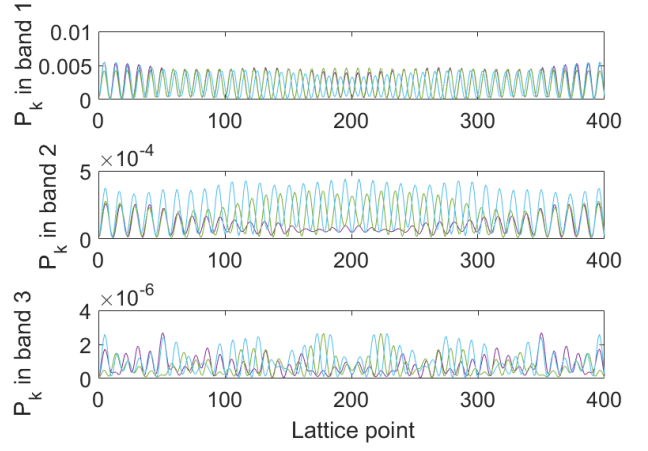
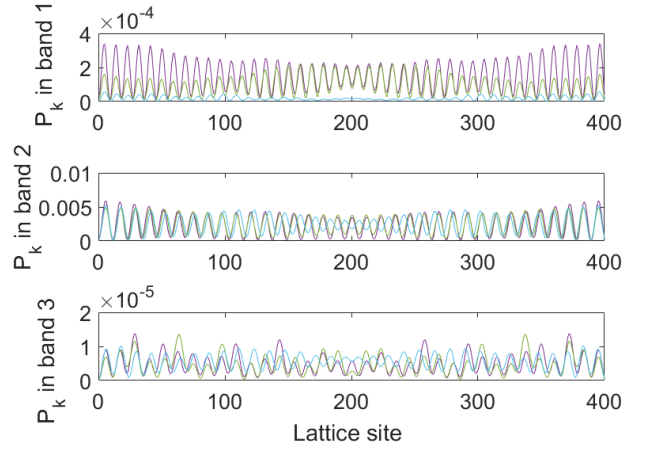
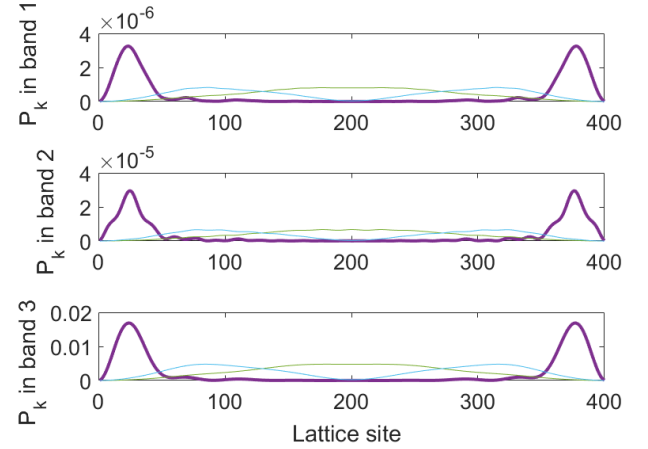
(a) Band 1  $P_k$ -functions.(b) Band 2  $P_k$ -functions.(c) Band 3  $P_k$ -functions.

FIG. 34: The occupational probability  $P_k$  of the six states closest to zero energy in the different bands with band interaction when  $\mu = -2t + 8E_{sb}$ . Other parameter values in Table IV.

TABLE V: Parameters used in the three-band Josephson junction model

$N$	$\Delta_{11}/\mu\text{eV}$	$\Delta_{22}/\mu\text{eV}$	$\Delta_{33}/\mu\text{eV}$	$\Delta_{12}/\mu\text{eV}$	$\Delta_{23}/\mu\text{eV}$	$\Delta_{13}/\mu\text{eV}$	$h_x/\mu\text{eV}$	$m^*/m_e$	$\alpha_R/\text{peV}$	$a/\text{nm}$	$L_x/\mu\text{m}$	$L_y/\text{nm}$	$t/\text{meV}$	$E_{sb}/\mu\text{eV}$
600	200	200	200	100	100	100	320	0.023	16	5	3	130	66.3	967

## V. MULTI-BAND JOSEPHSON JUNCTION

The last system that was simulated was a nanowire with three energy bands and a Josephson junction. This combines the three-band model from Section IV B with the Josephson junction system from Section III B, meaning that the Hamiltonian matrix was given by (28) with removed  $\Delta$ -terms and added  $V_g$  for the middle lattice sites like in (21).

The analysis for this system was focused on the energy barrier. By varying the size of the barrier separating the Majorana bound states closest to the junction, the barrier's impact on the eigenenergies of the Majorana bound states as well as the first excited states beyond those were investigated.

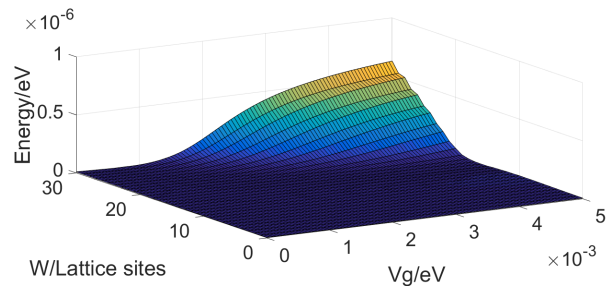
### A. Barrier Data

In the plots below, simulations were done in the same way as in previous sections, however this time the eigenenergies were plotted against the barrier height  $V_g$  and width  $W$  at the same time, resulting in 3D-plots. Previously in Fig. 13 in Section III B, the impact of the barrier height and width were only plotted separately. In order to more easily draw a parallel between these earlier plots and the 3D ones, 2D line plots along certain lines of the 3D plots are included in Fig. 38.

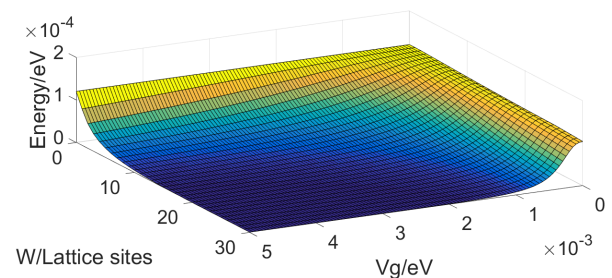
Beyond simply varying the voltage barrier, the chemical potential was also changed between simulations. The chemical potential was set to  $\mu = -2t$ ,  $\mu = -2t + 3E_{sb}$  and  $\mu = -2t + 8E_{sb}$ , meaning that all simulations were done at the bottom of all three of the energy bands in this model. Majorana bound states should appear in all of these bands, but as can be seen below the barrier's impact will differ depending on which value of  $\mu$  was used.

For all of the simulations below the parameters were given by Table V. The (a)-plots will show  $E_0$  on the y-axis and the (b)-plots will show  $E_M$  on the y-axis. The figures are also plotted with different scales on the z-axes, another important factor to keep in mind when comparing different plots.

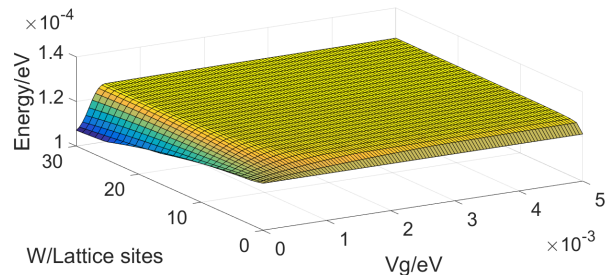
The edge states in Fig. 35a have zero energy even without the barrier since even then there are Majorana bound states at the edges of the wire. However as the barrier grows, their energy is increased. This is because as the barrier is increased, Majorana bound states will form in the middle of the wire whose wavefunctions will overlap with the states at the ends of the wire, thereby increasing their energy. The occupational probability of the four Majorana bound states were plotted in Fig. 12 in



(a) States at the ends of the wire.



(b) States forming at the Josephson junction. Note that the figure has been rotated in order to achieve the best view of the plot.



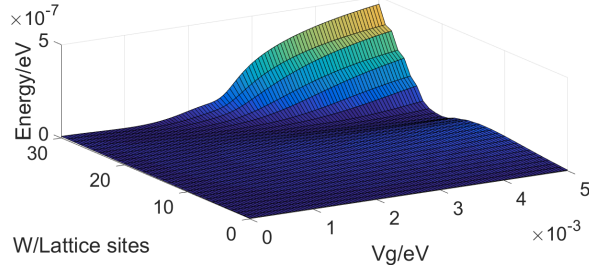
(c) First excited states.

FIG. 35: The eigenenergy of the three positive energy states closest to zero energy with  $\mu$  at the bottom of band 1 ( $\mu = -2t$ ) as a function of barrier width and barrier height. Parameters found in Table V.

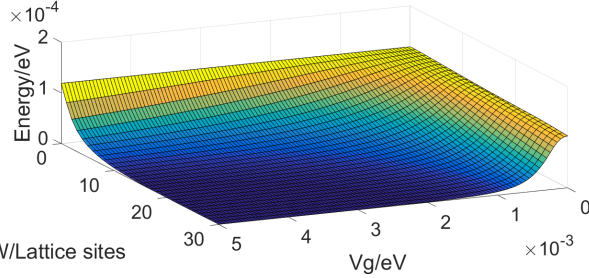
Section III B.

The Majorana bound states near the Josephson junction that start to form in Fig. 35b do not exist without a barrier, so the eigenenergies will therefore have a high energy when the barrier is low or thin and move towards a lower energy as the barrier grows.

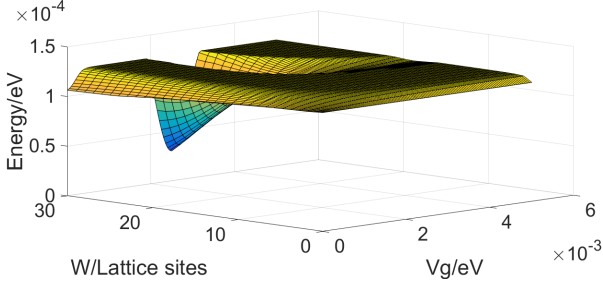
The excited state seen in Fig. 35c has a relatively constant energy. As soon as a barrier is introduced, its energy is raised and kept unchanged with further manipulation of the barrier.



(a) States at the ends of the wire.



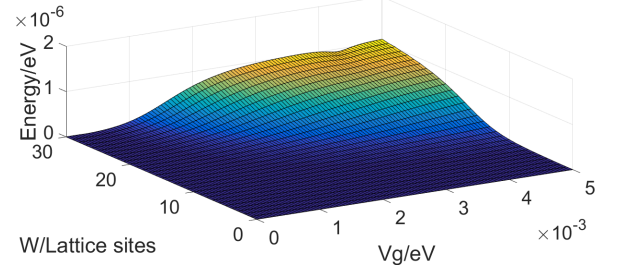
(b) States forming at the Josephson junction. Note that the figure has been rotated in order to achieve the best view of the plot.



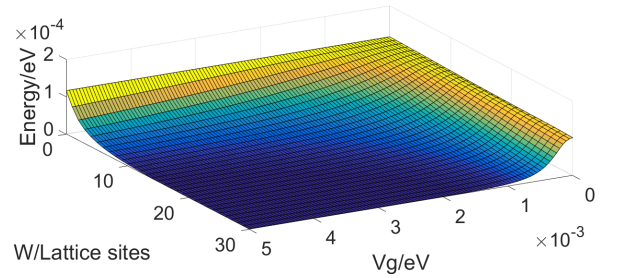
(c) First excited states.

FIG. 36: The eigenenergy of the three positive energy states closest to zero energy with  $\mu$  at the bottom of band 2 ( $\mu = -2t + 3E_{sb}$ ) as a function of barrier width and barrier height. Parameters found in Table V.

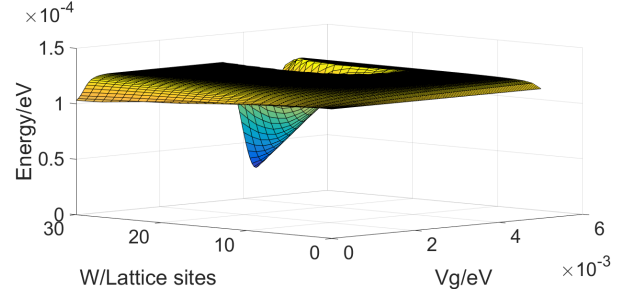
As  $\mu$  moves from the bottom of band 1 to the bottom of band 2 in Fig. 36, some differences are apparent. For the edge states in Fig. 36a, a small increase in energy will happen at around  $W = 10 - 20$  lattice sites. The states near the Josephson junction seen in Fig. 36b are very similar to the ones with  $\mu$  at the bottom of band 1 found in Fig. 35. For the first excited states in Fig. 36c, a dip in energy can be seen at high  $W$  between  $V_g = 2 - 3$  meV. This will make the energy gap between the Majorana bound states and the excited states smaller at these values.



(a) States at the ends of the wire.



(b) States forming at the Josephson junction. Note that the figure has been rotated in order to achieve the best view of the plot.



(c) First excited states.

FIG. 37: The eigenenergy of the three positive energy states closest to zero energy with  $\mu$  at the bottom of band 3 ( $\mu = -2t + 8E_{sb}$ ) as a function of barrier width and barrier height. Parameters found in Table V.

In Fig. 37  $\mu$  is changed to be at the bottom of band 3. In Fig. 37a there is a slight dip in energy at high values of  $W$  and  $V_g$ , around  $W = 30$  and  $V_g = 4$  meV. The eigenenergies of the states forming near the Josephson junction in Fig. 37b once again seem unchanged. In Fig. 37c there is a dip in energy for large  $W$  between  $V_g = 4 - 5$  meV.

In the interest of clarity, line plots have been done below in Fig. 38 for  $\mu$  at the bottom of bands 1, 2 and 3 (Fig. 35, 36 and 37) and for  $W = 20$  and  $W = 30$ . It is clear from these plots that the Majorana bound states that form by the Josephson junction will reach zero energy faster for a wider barrier. This is because the wavefunctions will decay exponentially within the barrier and a wider barrier will mean that the overlap between the Josephson junction states will go to zero quicker.

Other shapes of barriers were also simulated, this is shown in Appendix A. The shapes are trapezoidal and triangular and the results are qualitatively the same as with the rectangular barrier shown here.

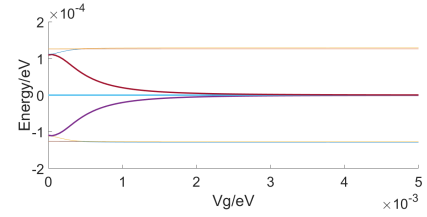
## B. Discussion

The most important thing when looking at the figures above is to see when the states that have the possibility of becoming Majorana bound states can do so, which means that they need to be close to zero energy. It is desirable for  $E_M$  to have a clear distinction between zero and finite energy and it is also important to keep  $E_0$  at zero energy. It is therefore wise to choose a  $W$  where it would be possible to manipulate the energy states that form the Majorana bound states near the Josephson junction to go between zero and finite energy with a small difference in  $V_g$  and without disrupting the Majorana bound states at the edges of the wire.

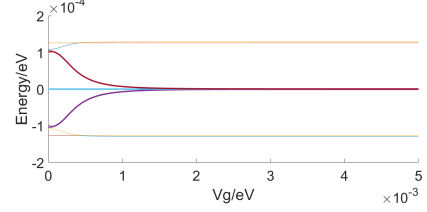
Another factor to look at are the excited states. For reasons that will be explained in the next section, the excited states need to have as large of an energy gap as possible to the Majorana states. It is therefore a cause for concern that some excited states have dips in energy for certain barrier parameters. Fig. 38 does show that there are parameter choices that can be made to limit the impact of these dips in energy. For example in Fig. 38f the energy dip is at a high enough value of  $V_g$  that it can be easily avoided. It is worth noting that these dips in energy only exist in higher bands, which is why they were not visible in Fig. 13a before the multi-band model was introduced.

From the plots above it is clear that the states will behave differently when  $\mu$  is in a different energy band. The clearest examples are the excited states; with  $\mu$  at the bottom of band 1 they are relatively constant while for other values of  $\mu$  they will have dips in energy for certain parameter values. The edge states with  $\mu$  at the bottom of band 3 seen in Fig. 37a gain in energy faster and reach a higher maximum compared to the other values of  $\mu$ , the energy at  $W = 30$  and  $V_g = 5$  meV for Fig. 37a with  $\mu$  at the bottom of band 3 is over twice as high as for Fig. 36a with  $\mu$  at the bottom of band 2.

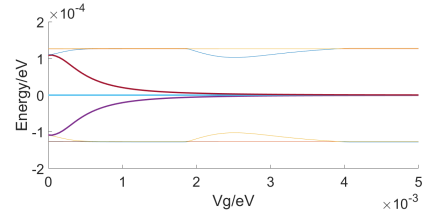
The impact that the shape of the barrier has on the results can be seen in Appendix A. While there are clear differences that can primarily be seen for the triangular barrier, they all share the same general shape and a lot of the differences are merely due to the limit in which



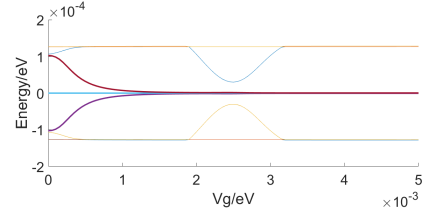
(a) Band 1,  $W = 20$ .



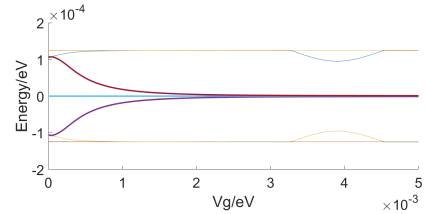
(b) Band 1,  $W = 30$ .



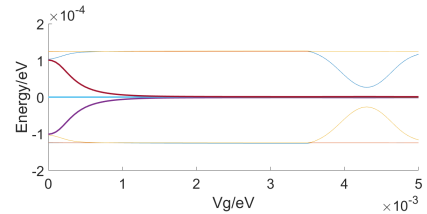
(c) Band 2,  $W = 20$ .



(d) Band 2,  $W = 30$ .



(e) Band 3,  $W = 20$ .



(f) Band 3,  $W = 30$ .

FIG. 38: Line plot of the energy of the ten eigenenergies closest to zero with  $\mu$  at the bottom of all of the three bands as a function of barrier height with a fixed width. Parameters found in Table V.

the simulations have been done. The result that can be seen here is that while the shape of the barrier does not completely change the behavior of the states, it will tune the impact of the different barrier parameters.

## VI. OUTLOOK AND CONCLUSIONS

In this thesis I have used single- and multi-band models to simulate systems with and without a Josephson junction with a semiconducting nanowire with proximity-induced superconductivity and strong spin-orbit coupling. This has been used to track the presence of Majorana bound states in these systems. The thesis started with a simple model and gradually increased in complexity, all the while showing how the eigenenergies, occupational probability along the nanowire and magnetic field dependence will change in each model. For the multi-band model it was also shown how the band interaction terms will influence the Majorana bound states.

After introducing the different models that the system is built upon, the final system with both a Josephson junction and a three-band model was analyzed specifically in regards to the impact that the Josephson junction has on the Majorana bound states closest to the junction. This is relevant because by analyzing both the Majorana coupling energy  $E_M$  and the excited states in the system, it is possible to optimize a barrier that will allow for good control and fast operations.

To this end, consider a system where the width of the barrier is fixed at manufacturing and the height of the barrier will be switched between zero and a maximum height. This switch represents a voltage applied to the system.

The ideal case in this investigated system is one where the only significantly affected states are the Majorana bound states at the Josephson junction, and where these states change very quickly as a function of  $V_g$ . This would allow a clear signal of when the system is turned off and on as well as allow for quick computations. It is therefore wise to choose a width of the barrier that leads to a large difference in  $E_M$  for a small difference in  $V_g$ . From the plots in Fig. 38 all values of  $E_M$  between the topological energy gap to essentially zero are achievable, it is just a matter of parameter choices.

The excited states will affect the time scale of the operations that are performed on the system. Energy is related to time according to  $\Delta E = \frac{\hbar}{\Delta T}$ . If an operation is performed on the system with a time scale faster than the corresponding energy of the energy gap to the first excited states, these states can be occupied which will cause computational errors. To get a better idea of the time scale that the dips in energy of the excited states have, let us look closer at Fig. 38d. The energy gap to the excited states for  $V_g = 1.9$  meV and  $V_g = 2.5$  meV is 125  $\mu$ eV and 30  $\mu$ eV, respectively. This corresponds

to 5.27 ps and 21.9 ps. These time scales are very small and it could therefore be difficult to operate a practical system at a speed where this dip in energy would be relevant. This means that the energy dips seen are not of relevant concern for today's technology. It is worth mentioning that if these high speeds were to be reached, a difference in efficiency of 4 times is a very big change.

After analyzing the different line plots in Fig. 38, it is clear that there exists a  $W$  where good control over the states near the Josephson junction is possible. One can see that by choosing a larger barrier width of  $W = 30$ , the system will react faster, however the excited states can be a lot more troublesome. By choosing a slightly smaller width of  $W = 20$ , the system will become more stable with regards to the excited states, however larger voltage range would also be required in order to get a strong on/off signal.

It is clear from the plots in the above section that the excited states were more stable when  $\mu$  is at the bottom of band 1,  $\mu = -2t$ . While it would be very beneficial, it could be difficult to achieve a practical system where the chemical potential stays at the bottom of band 1. At this  $\mu$  there are fewer electrons that can screen disturbances. This leads to sharp changes in  $\mu$  that are difficult to keep within the range that allows for Majorana bound states.

This analysis has only been done for one specific system, so it is therefore unclear if these results will appear in a more general case. In addition, the models used are simple approximations of a very complex system, including the tight binding model that this entire study is based upon. The models used can be improved by for example including more precise electrostatics and adding random disorder and more energy bands. The dips in energy for the excited states seen for example in Fig. 36c happen only for the multi-band system. Further analysis of why it only happens in higher energy bands is not done in this thesis and could be an interesting subject for further research.

In this thesis I have shown that the choice of barrier parameters for a Josephson junction to adequately separate the nearest Majorana bound states is non-trivial. I have also shown that it is possible to choose them in a way that improves control over the system depending on the operational requirements. The results point to a general length scale for the barrier width (between 50 and 200 nm) and height (between 2 and 5 meV) of Josephson junctions in order to have good control. Finally they predict a general trend that the excited states vary less with changes in  $W$  and  $V_g$  when  $\mu$  is at the bottom of band 1.

## ACKNOWLEDGEMENTS

The author would like to thank his supervisors Martin Leijnse and Michael Hell for their helpful advice throughout this project.

- 
- [1] Sumanta Tewari, S Das Sarma, Chetan Nayak, Chuanwei Zhang, and P Zoller. Quantum computation using vortices and majorana zero modes of a p x+ i p y superfluid of fermionic cold atoms. *Physical review letters*, 98(1):010506, 2007.
- [2] Martin Leijnse and Karsten Flensberg. Introduction to topological superconductivity and majorana fermions. *Semiconductor Science and Technology*, 27(12):124003, 2012.
- [3] Frank Wilczek. Majorana returns. *Nature Physics*, 5:614–618, 2009.
- [4] Jason Alicea, Yuval Oreg, Gil Refael, Felix von Oppen, and Matthew PA Fisher. Non-abelian statistics and topological quantum information processing in 1d wire networks. *Nature Physics*, 7(5):412–417, 2011.
- [5] Chetan Nayak, Steven H Simon, Ady Stern, Michael Freedman, and Sankar Das Sarma. Non-abelian anyons and topological quantum computation. *Reviews of Modern Physics*, 80(3):1083, 2008.
- [6] Sergey Bravyi. Universal quantum computation with the  $\nu = 5/2$  fractional quantum hall state. *Phys. Rev. A*, 73:042313, Apr 2006.
- [7] G De Lange, B Van Heck, A Bruno, DJ Van Woerkom, A Geresdi, SR Plissard, EPAM Bakkers, AR Akhmerov, and L DiCarlo. Realization of microwave quantum circuits using hybrid superconducting-semiconducting nanowire josephson elements. *Physical review letters*, 115(12):127002, 2015.
- [8] TW Larsen, KD Petersson, F Kuemmeth, TS Jespersen, P Krogstrup, Jesper Nygård, and CM Marcus. Semiconductor-nanowire-based superconducting qubit. *Physical review letters*, 115(12):127001, 2015.
- [9] Herbert Fröhlich. Theory of the superconducting state. i. the ground state at the absolute zero of temperature. *Physical Review*, 79(5):845, 1950.
- [10] C. C. Tsuei and J. R. Kirtley. Pairing symmetry in cuprate superconductors. *Rev. Mod. Phys.*, 72:969–1016, Oct 2000.
- [11] Patrick A Lee and Xiao-Gang Wen. Spin-triplet p-wave pairing in a three-orbital model for iron pnictide superconductors. *Physical Review B*, 78(14):144517, 2008.
- [12] Yuki Nagai, Hiroki Nakamura, and Masahiko Machida. Quasiclassical treatment and odd-parity/triplet correspondence in topological superconductors. *Journal of the Physical Society of Japan*, 83(5):053705, 2014.
- [13] Sumanta Tewari, S Das Sarma, Chetan Nayak, Chuanwei Zhang, and P Zoller. Quantum computation using vortices and majorana zero modes of a p x+ i p y superfluid of fermionic cold atoms. *Physical review letters*, 98(1):010506, 2007.
- [14] Liang Fu and C. L. Kane. Superconducting proximity effect and majorana fermions at the surface of a topological insulator. *Phys. Rev. Lett.*, 100:096407, Mar 2008.
- [15] P. G. De Gennes. Boundary effects in superconductors. *Rev. Mod. Phys.*, 36:225–237, Jan 1964.
- [16] B Pannetier and H Courtois. Andreev reflection and proximity effect. *Journal of low temperature physics*, 118(5-6):599–615, 2000.
- [17] A. Manchon, H. C. Koo J. Nitta S. M. Frolov & R. A. Duine. New perspectives for rashba spin-orbit coupling. *Nature Materials*, 14:871–882, 2015.
- [18] Branislav K Nikolić, Liviu P Zârbo, and Satofumi Souma. Mesoscopic spin hall effect in multiprobe ballistic spin-orbit-coupled semiconductor bridges. *Physical Review B*, 72(7):075361, 2005.
- [19] M. Madsen F. Kuemmeth T. S. Jespersen J. Nygård P. Krogstrup C.M. Marcus S. M. Albrecht, A. P. Higginbotham. Exponential protection of zero modes in majorana islands. *Nature*, 531:206–209, 2016.
- [20] J Knobbe and Th Schäpers. Magnetosubbands of semiconductor quantum wires with rashba spin-orbit coupling. *Physical Review B*, 71(3):035311, 2005.
- [21] T D Stanescu and S Tewari. Majorana fermions in semiconductor nanowires: fundamentals, modeling, and experiment. *Journal of Physics: Condensed Matter*, 25(23):233201, 2013.
- [22] A Yu Kitaev. Unpaired majorana fermions in quantum wires. *Physics-Uspekhi*, 44(10S):131, 2001.
- [23] Anindya Das, Yuval Ronen, Yonatan Most, Yuval Oreg, Moty Heiblum, and Hadas Shtrikman. Zero-bias peaks and splitting in an al-inas nanowire topological superconductor as a signature of majorana fermions. *Nature Physics*, 8(12):887–895, 2012.
- [24] S. Das Sarma, Jay D. Sau, and Tudor D. Stanescu. Splitting of the zero-bias conductance peak as smoking gun evidence for the existence of the majorana mode in a superconductor-semiconductor nanowire. *Phys. Rev. B*, 86:220506, Dec 2012.
- [25] David Aasen, Michael Hell, Ryan V. Mishmash, Andrew Higginbotham, Jeroen Danon, Martin Leijnse, Thomas S. Jespersen, Joshua A. Folk, Charles M. Marcus, Karsten Flensberg, and Jason Alicea. Milestones toward majorana-based quantum computing. *Phys. Rev. X*, 6:031016, Aug 2016.
- [26] Michael Hell, Jeroen Danon, Karsten Flensberg, and Martin Leijnse. Time scales for majorana manipulation using coulomb blockade in gate-controlled superconducting nanowires. *Phys. Rev. B*, 94:035424, Jul 2016.
- [27] Jason Alicea. New directions in the pursuit of majorana fermions in solid state systems. *Reports on Progress in Physics*, 75(7):076501, 2012.
- [28] Roman M Lutchyn and Matthew PA Fisher. Interacting topological phases in multiband nanowires. *Physical Review B*, 84(21):214528, 2011.
- [29] Girish Sharma and Sumanta Tewari. Tunneling conductance for majorana fermions in spin-orbit coupled semiconductor-superconductor heterostructures using superconducting leads. *Physical Review B*, 93(19):195161, 2016.
- [30] Roman M. Lutchyn, Tudor D. Stanescu, and S. Das Sarma. Search for majorana fermions in multiband semiconducting nanowires. *Phys. Rev. Lett.*, 106:127001, Mar 2011.

## Appendix A: Barrier Shapes

Three different shapes of barriers were simulated. This is because in a real system the shape of the barrier could be different depending on various experimental factors and different cases are studied in order to verify that the conclusions reached in Section VI are not only valid for a specific barrier shape. The one shown in Section V A was a simple, rectangular shape where the height of the barrier was  $V_g$  for the entire width of the barrier, see Fig. 39a. The first other shape that was simulated was a trapezoidal shape where only 1/3 of the barrier was the height of  $V_g$  and the other two thirds were linear slopes from 0 to  $V_g$ , see Fig. 39b. Finally the third shape that was simulated was a triangular shape where only the middle lattice site, if it existed, was  $V_g$  and the entire rest of the barrier was a slope from 0 to  $V_g$ , see Fig. 39c. Note that no matter the shape of the barrier, there is no induced superconductivity for the entire width of the barrier.

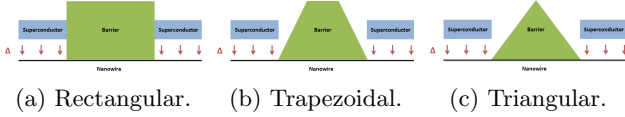
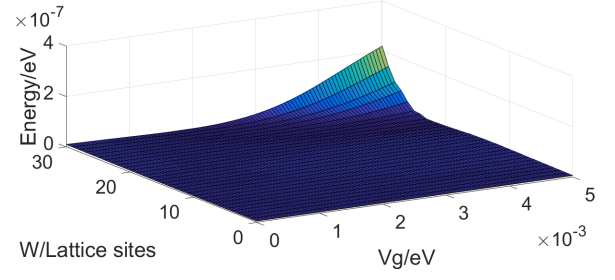
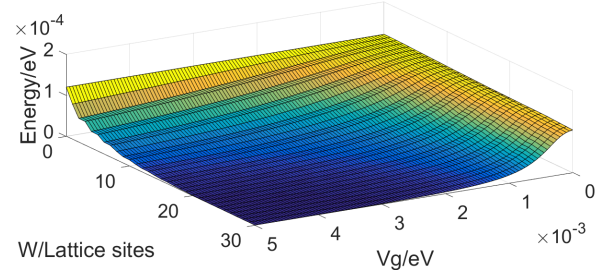


FIG. 39: Shapes of barriers.

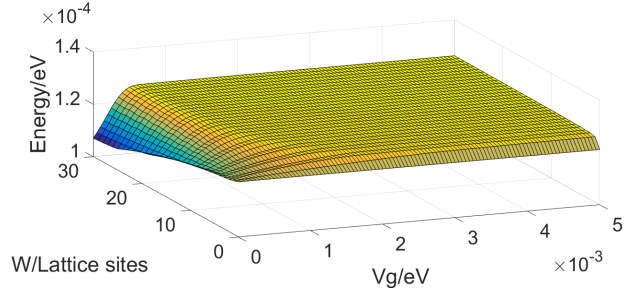
### 1. Trapezoidal Barrier



(a) States at the ends of the wire.



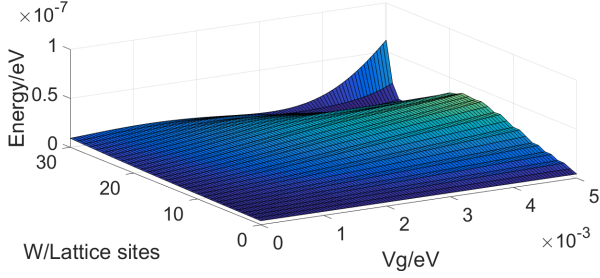
(b) States forming at the Josephson junction. Note that the figure has been rotated in order to achieve the best view of the plot.



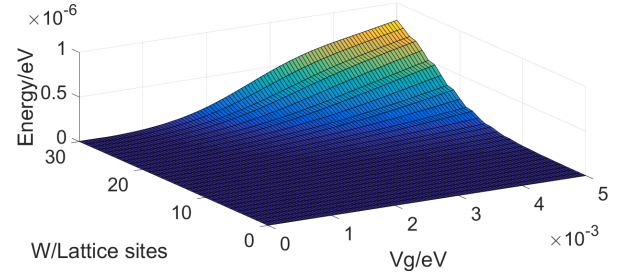
(c) First excited state.

FIG. 40: The eigenenergy of the three positive energy states closest to zero energy with  $\mu$  at the bottom of band 1 ( $\mu = -2t$ ) for a trapezoidal barrier. Parameters found in Table V.

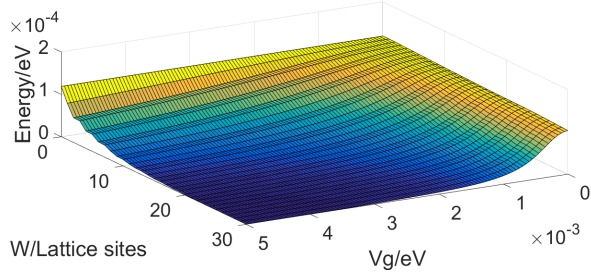
As we look at the differences between the rectangular and the trapezoidal barrier with  $\mu$  at the bottom of band 1, it is clear that band 1 is not significantly affected.



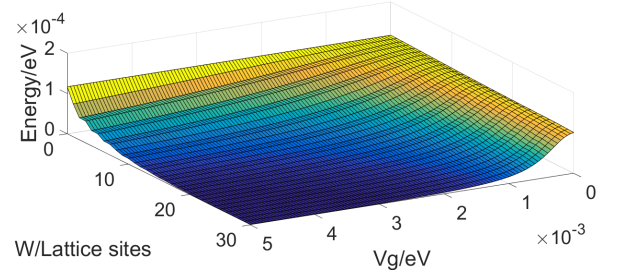
(a) States at the ends of the wire.



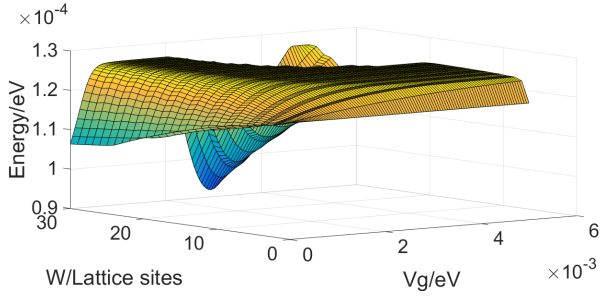
(a) States at the ends of the wire.



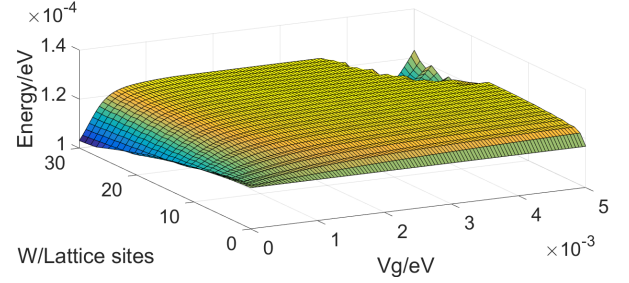
(b) States forming at the Josephson junction. Note that the figure has been rotated in order to achieve the best view of the plot.



(b) States forming at the Josephson junction. Note that the figure has been rotated in order to achieve the best view of the plot.



(c) First excited state.



(c) First excited state.

FIG. 41: The eigenenergy of the three positive energy states closest to zero energy with  $\mu$  at the bottom of band 2 ( $\mu = -2t + 3E_{sb}$ ) for a trapezoidal barrier. Parameters found in Table V.

FIG. 42: The eigenenergy of the three positive energy states closest to zero energy with  $\mu$  at the bottom of band 3 ( $\mu = -2t + 8E_{sb}$ ) for a trapezoidal barrier. Parameters found in Table V.

The differences between the barrier shapes become more apparent when looking at Fig. 41. The same general features are there, such as the large dip in energy in Fig. 41c for certain values of  $V_g$ . It is apparent though that these features are distorted when compared to the same irregularities in Fig. 36.

In Fig. 42c, we now see a new irregularity. For high  $W > 10$ , there is a range of  $V_g = 1 - 4$  meV values where the excited state is at high energy and stable, but for large and small  $V_g$  the energy drops. This drop is not as big of a drop as with the rectangular barrier in Section V A, however the dip seems to be cut off at  $V_g = 5$  meV.

Line plots have once again been done in Fig. 43, however this time only for bands 2 and 3 (Fig. 41 and 42) and for  $W = 20$  and  $W = 30$ .

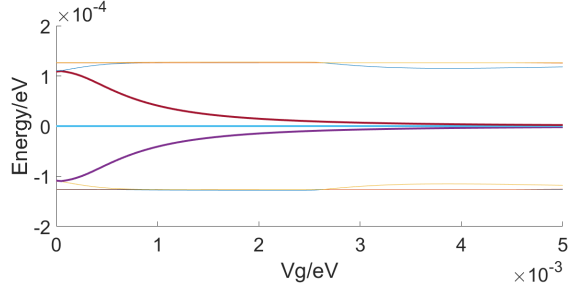
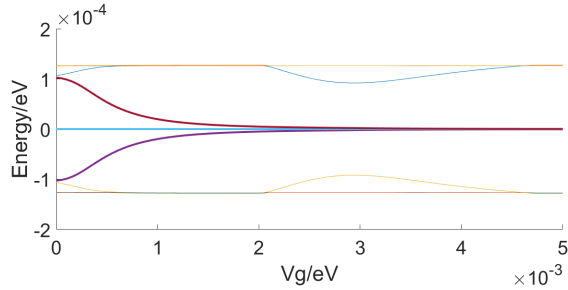
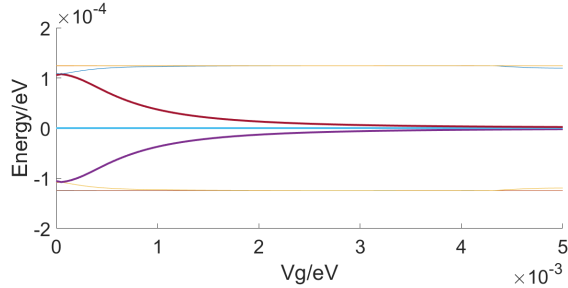
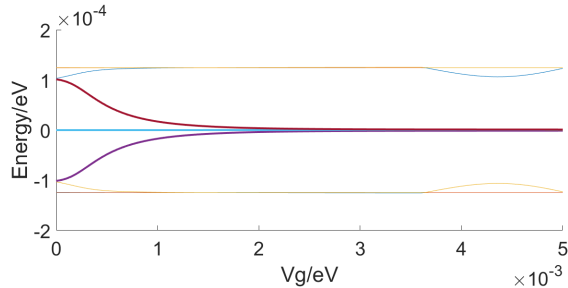
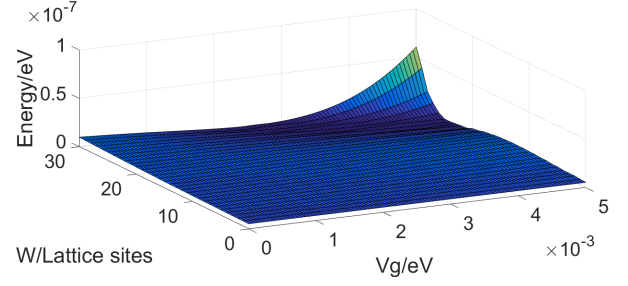
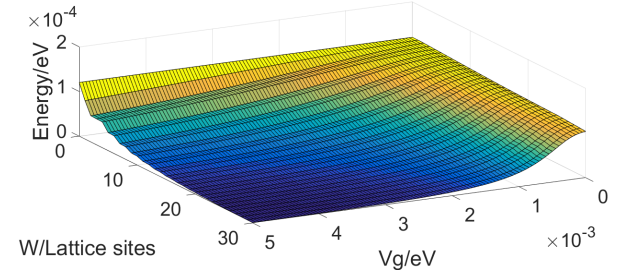
(a) Band 2,  $W = 20$ .(b) Band 2,  $W = 30$ .(c) Band 3,  $W = 20$ .(d) Band 3,  $W = 30$ .

FIG. 43: Line plot of the energy of the ten eigenenergies closest to zero with  $\mu$  at the bottom of bands 2 and 3 with a trapezoidal barrier as a function of barrier height with a fixed width. Parameters found in Table V.

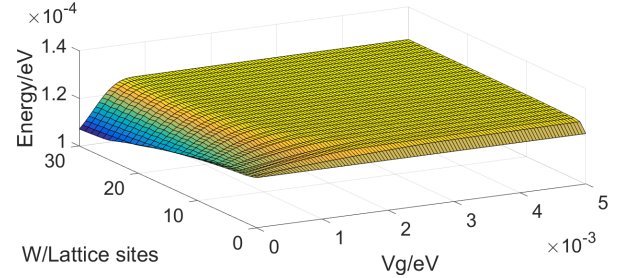
## 2. Triangular Barrier



(a) States at the ends of the wire.



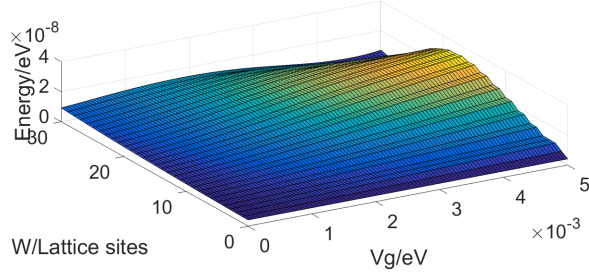
(b) States forming at the Josephson junction. Note that the figure has been rotated in order to achieve the best view of the plot.



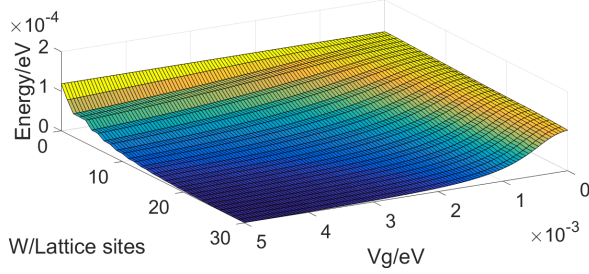
(c) First excited state.

FIG. 44: The eigenenergy of the three positive energy states closest to zero energy with  $\mu$  at the bottom of band 1 ( $\mu = -2t$ ) for a triangular barrier. Parameters found in Table V.

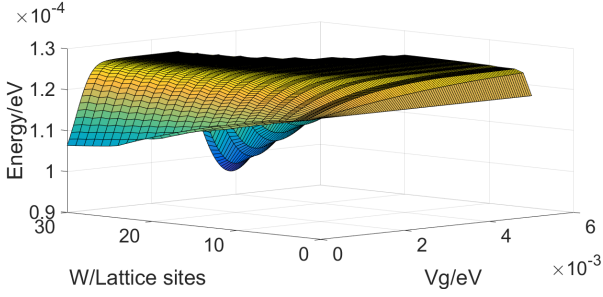
In Fig. 44 the triangular barrier is introduced with  $\mu$  at the bottom of band 1. In Fig. 44a the height of the energy peak at high values of  $W$  and  $V_g$  corresponding to an overlap with the newly formed Majorana bound states near the Josephson junction is roughly 10 times smaller than the corresponding peak for other barrier shapes. This higher peak is probably a result of the effect that different shapes of the barrier will tune the parameter impact differently. This high peak can be reached with the rectangular and trapezoidal barrier, but it would require higher values of  $W$  and  $V_g$ .



(a) States at the ends of the wire.



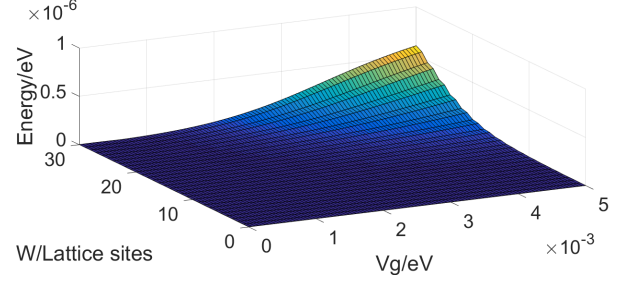
(b) States forming at the Josephson junction. Note that the figure has been rotated in order to achieve the best view of the plot.



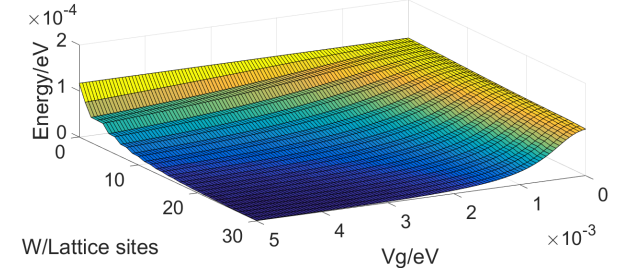
(c) First excited state.

FIG. 45: The eigenenergy of the three positive energy states closest to zero energy with  $\mu$  at the bottom of band 2 ( $\mu = -2t + 3E_{sb}$ ) for a triangular barrier. Parameters found in Table V.

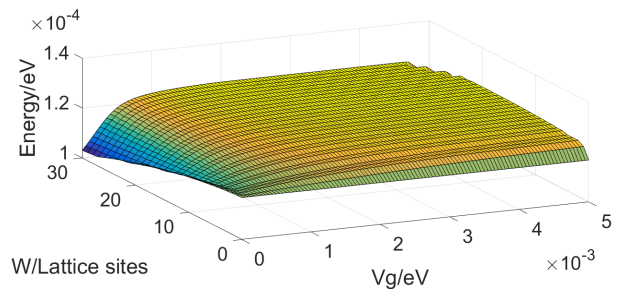
There seems to be a high energy peak missing in Fig. 45a for high values of  $W$  and  $V_g$ , compared to the corresponding plots for different barrier shapes in Fig. 36a and 41a, however it would probably be seen at values of  $W$  and  $V_g$  higher than the limit of this plot. The increase in energy for certain values of  $W$  with  $\mu$  at the bottom of band 2 that was first seen in Fig. 36a can be seen clearly at  $W = 10 - 20$  and  $V_g > 3$  meV.



(a) States at the ends of the wire.



(b) States forming at the Josephson junction. Note that the figure has been rotated in order to achieve the best view of the plot.

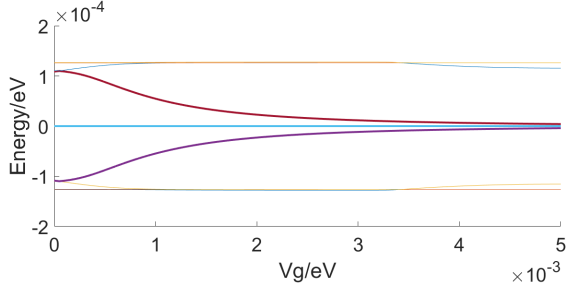


(c) First excited state.

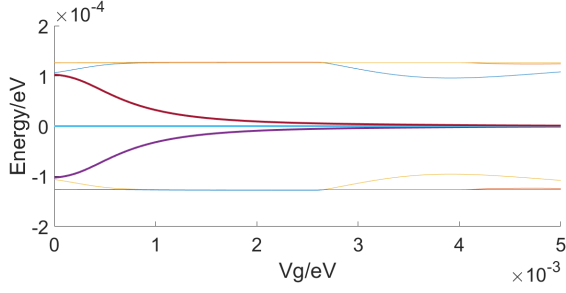
FIG. 46: The eigenenergy of the three positive energy states closest to zero energy with  $\mu$  at the bottom of band 3 ( $\mu = -2t + 8E_{sb}$ ) for a triangular barrier. Parameters found in Table V.

The plots in Fig. 46 are similar to the ones in Fig. 42, which is reasonable as they both have  $\mu$  at the bottom of band 3. Similarly to Fig. 42c, there is a range of parameter values where the excited state is at high energy and stable for Fig. 46c, however for the trapezoidal barrier the range is roughly given by  $W > 10$  and  $V_g = 1 - 4$  meV and for the triangular barrier the range is roughly given by  $W = 10 - 25$  and  $V_g > 2$ .

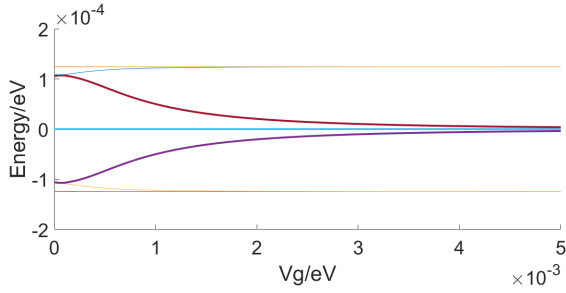
Line plots have once again been done in Fig. 47 for  $\mu$  at the bottom of bands 2 and 3 (Fig. 45a and 46) and for  $W = 20$  and  $W = 30$ .



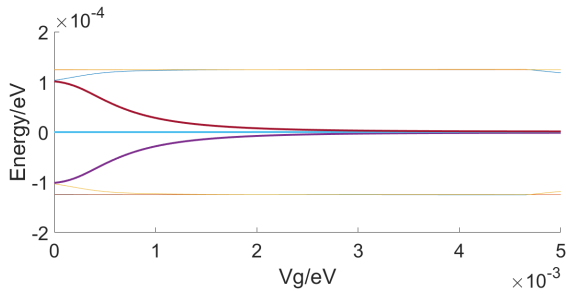
(a) Band 2,  $W = 20$ .



(b) Band 2,  $W = 30$ .



(c) Band 3,  $W = 20$ .



(d) Band 3,  $W = 30$ .

FIG. 47: Line plot of the energy of the ten eigenenergies closest to zero with  $\mu$  at the bottom of bands 2 and 3 with a triangular barrier as a function of barrier height with a fixed width. Parameters found in Table V.